

Article 4 :

Publié dans la revue : *Mechanics of Advanced Materials and Structures*.

- Éditeur : Taylor & Francis
- ISSN : 1537-6494 E-ISSN : 1537-6532
- Période de couverture par Scopus : 1997, puis de 2001 à 2025
- Lien d'article Doi : <https://doi.org/10.1080/15376494.2025.2473687>
- Domaines scientifiques : Génie civil et génie structurel ; Mécanique des matériaux
- Type de source : Revue scientifique (journal classé A)
- Impact factor : 6.6 (2024);
- Type de source : Revue classée A (*lien* : https://www.dgrsdt.dz/fr/revues_A?search=Mechanics+of+Advanced+Materials+and+Structures)



A screenshot of the DGRS DT website's search results page for scientific journals. The header includes the logo 'DGRS DT' and the Arabic text 'المديرية العامة للبحث العلمي والتطوير التكنولوجي'. It features a navigation bar with links to Accueil, DGRS DT, Activités R&D, DEV_TECH, Revues scientifiques, Services, Contact, and a search icon. Below the header is a banner with several journal covers, including 'Nature', 'Science Advances', and 'Nature Nanotechnology'. The main title 'Revues scientifiques de catégorie A' is displayed prominently. Below it, a breadcrumb navigation shows 'Accueil → revues_A'. The page content includes a section titled 'Revues scientifiques' and 'Liste des revues scientifiques de catégorie A'. A search bar at the top is filled with 'Mechanics of Advanced Materials and Structures'. The results table has columns for 'TITRE DE LA REVUE--', 'EDITEUR', 'ISSN', and 'EISSN'. The first result listed is 'MECHANICS OF ADVANCED MATERIALS AND STRUCTURES' by 'TAYLOR & FRANCIS INC' with ISSN 1537-6494 and EISSN 1537-6532. There is also a 'Télécharger' button with a cloud icon.

[Submit an article](#)[Journal homepage](#)

110

Views

1

CrossRef
citations to date

0

Altmetric

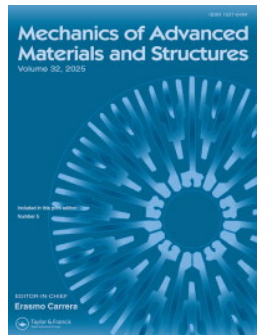
ORIGINAL ARTICLE

A novel strain-based approach with high-order shear deformation for enhanced static and buckling performance of functionally graded plates

Madjda Chenafi , Messaoud Bourezane , Taqiyeddine Assas & Abdelouahab Tati

Received 16 Jan 2025, Accepted 23 Feb 2025, Published online: 06 Mar 2025

 Cite this article <https://doi.org/10.1080/15376494.2025.2473687>



A novel strain-based approach with high-order shear deformation for enhanced static and buckling performance of functionally graded plates

Madjda Chenafi, Messaoud Bourezane, Taqiyeddine Assas & Abdelouahab Tati

To cite this article: Madjda Chenafi, Messaoud Bourezane, Taqiyeddine Assas & Abdelouahab Tati (06 Mar 2025): A novel strain-based approach with high-order shear deformation for enhanced static and buckling performance of functionally graded plates, *Mechanics of Advanced Materials and Structures*, DOI: [10.1080/15376494.2025.2473687](https://doi.org/10.1080/15376494.2025.2473687)

To link to this article: <https://doi.org/10.1080/15376494.2025.2473687>



Published online: 06 Mar 2025.



Submit your article to this journal



View related articles



CrossMark

View Crossmark data

ORIGINAL ARTICLE

A novel strain-based approach with high-order shear deformation for enhanced static and buckling performance of functionally graded plates

Madjda Chenafi^a , Messaoud Bourezane^a , Taqiyeddine Assas^a , and Abdelouahab Tati^b 

^aLaboratoire d'Aménagements Hydrauliques et Environnement (LAHE), Département de Génie Civil et Hydraulique, Université de Biskra, Biskra, Algeria; ^bLaboratoire de Génie Energétique et Matériaux (LGEM), Département de Génie Civil et Hydraulique, Université de Biskra, Biskra, Algeria

ABSTRACT

This work presents the first study investigating the static and buckling behavior of functionally graded rectangular plates using a strain-based approach combined with high-order shear deformation theory and a newly developed sinusoidal function. The novelty of this study lies in the development of a novel sinusoidal function for high-order shear deformation theory, the application of the strain-based approach within this framework, and the combination of these methods for the analysis of functionally graded plates. The sinusoidal function, derived by comparing the energy of shear deformation based on three-dimensional elasticity theory and Reissner–Mindlin theory, plays a critical role in reducing the number of unknowns from six to five. This reduction is achieved by enforcing zero transverse shear stress at the top and bottom surfaces and assuming a sinusoidal distribution of transverse shear strains through the thickness. The material properties of the functionally graded plate vary through the thickness according to a power-law distribution. The resulting element, a superposition of membrane and bending elements, eliminates membrane-bending coupling through the neutral plane concept. Stiffness and geometric matrices are derived using the potential energy principle. A parametric study is conducted to investigate the effects of key parameters on the static and buckling behavior of the plates. Numerical results, validated against literature using various meshes, demonstrate the accuracy and reliability of the proposed method for both static and buckling analyses. This work provides a robust and efficient tool for analyzing functionally graded plates in engineering applications such as aerospace, automotive, and civil structures.

ARTICLE HISTORY

Received 16 January 2025
Accepted 23 February 2025

KEYWORDS

Static; buckling behavior;
functionally graded plate;
strain-based approach;
high-order shear
deformation theory

1. Introduction

Functionally Graded Plates (FGPs) are composite structures characterized by a gradual variation in material properties across their thickness. This gradient can be engineered to achieve specific mechanical, thermal, or other functional characteristics, making FGPs suitable for various applications in engineering and materials science. FGPs are used in fields ranging from aerospace to biomedical engineering, offering enhanced performance and adaptability to diverse operational conditions [1]. The analysis of FGPs employs several advanced methodologies to understand their behavior under various conditions. The Finite Element Method (FEM) is a crucial analytical tool for studying FGPs, enabling detailed modeling of their complex behavior. It is particularly advantageous for FGPs due to its ability to handle complex geometries and varying material properties that characterize these plates. Advanced FEM models have significantly improved the accuracy of predicting bending, vibration, and stability behaviors, validating results against higher-order theories and experimental data [2–5].

The analysis of FGPs has significantly advanced with the development of shear deformation theories, notably the first-order shear deformation theory (FSDT) and higher-order shear deformation theories (HSDT). FSDT, introduced by Reissner and Mindlin [6], accounts for transverse shear deformation with a linear shear strain distribution across the thickness. This approach is efficient for thin and moderately thick plates, though it requires a shear correction factor to compensate for inaccuracies arising from its assumptions. This theory has been extensively adopted in the academic community as a robust analytical framework for investigating the mechanical behavior of FGPs. It has been widely applied in static bending and free vibration analyses, offering reasonable accuracy for various boundary conditions (BCs) and loading scenarios [7]. Additionally, FSDT has proven effective in examining the buckling behavior of FGPs, leveraging its ability to capture the influence of material gradation properties, making it a cornerstone in advanced plate mechanics [8–11]. In contrast, HSDTs provide a more detailed representation by incorporating nonlinear variations of in-plane and transverse displacements

through the plate thickness. This eliminates the need for shear correction factors, making HSDTs particularly effective for analyzing thick plates or those with steep material property gradients. They enable precise predictions of deflection and stress distributions. Recent advancements in HSDT formulations have further enhanced their accuracy by including effects such as stretching and higher-order shear deformations, improving predictions of both static and dynamic behaviors under complex loading conditions [12].

To address the limitations of shear correction factors, the HSDT initially introduced by Reddy [13], has been widely explored for the static, buckling, and free vibration analyses of FGPs. Matsunaga [14] developed a two-dimensional (2D) HSDT to investigate the characteristic frequencies and buckling stresses of FGPs, while Zenkour [15] proposed an analytical approach using sinusoidal shear deformation theory (SSDT) for their bending behavior. Another study [16] applied Reddy's third-order shear deformation theory (TSĐT) to derive an analytical method for free vibration analysis of square plates on elastic foundations. Similarly, another paper introduced a refined plate theory (RPT) based on HSDT with four unknowns, focusing on both static and dynamic responses [17]. Another study developed 2D and quasi-3D shear deformation theories for the static and free vibration analysis of FGPs, with inhomogeneous material properties. The governing equations were derived using Hamilton's principle, and the method's accuracy was validated through comparisons with existing solutions in the literature [18]. Further contributions detailed evaluation of the vibrational and static responses of rectangular and square FGPs [19]. In more recent studies, Tati introduced a finite element (FE) formulation with four nodes and five variables to examine functionally graded (FG) plate bending [20] and later expanded this work to analyze buckling behavior [21]. Sadgui and Tati proposed a novel TSĐT for dynamic and stability analyses [22], while a five-unknown HSDT was employed in another recent study to investigate the bending and free vibration of FG circular plates [23]. These advancements underscore the ongoing efforts to refine HSDT-based models for FGPs under various mechanical and BCs. Studies often investigate the critical buckling loads, considering different material gradation profiles and BCs. Zenkour studied the mechanical buckling of a rectangular FG plate using a refined higher-order shear and normal deformation theory, considering the impact of transverse normal strain [24]. Thai and Choi presented a refined theory for the buckling analysis of FGPs, which accounts for a quadratic variation of transverse shear strains and satisfies zero traction BCs without using shear correction factors [25]. In Reddy's study, analytical formulations and solutions for the buckling analysis of simply supported FGPs were presented using HSDT [26]. Recent research focused on the thermal post-buckling behavior of rectangular FGPs under large displacements, using FEM based on the Carrera Unified Formulation [27]. Another study investigated the buckling and post-buckling behavior of porous FGPs using a high-order continuation method combined with the FEM [28].

Numerous studies have significantly advanced the development of HSDT and their application to FGMs. Classical works, such as Levy [29] and Stein [30], laid the foundation for plate and beam theories, while recent research has expanded these concepts to address more complex behaviors. Studies on buckling, free vibration, and bending-stretching coupling in FG sandwich plates, as well as investigations into zig-zag effects, porosity, and thermo-mechanical responses in FG structures [31–38], have provided critical insights. Additionally, advanced theories incorporating trigonometric, hyperbolic, and quasi-3D deformations have been developed to analyze stress distribution, nonlinear vibrations, and static responses in FG plates, shells, and beams [39–41]. Furthermore, static analysis of FGPs resting on variable elastic foundations under various BCs has also received significant attention in the literature, contributing to a deeper understanding of the influence of foundation characteristics on the behavior of FG structures [42]. These works have collectively advanced the understanding and application of HSDT and FGM in modern structural analysis.

Unlike the traditional displacement-based approach, where displacements are the primary unknowns and strains are derived from them, the strain-based approach directly models strains as independent variables. This approach offers greater accuracy in capturing complex deformation behaviors, particularly for advanced materials like FGPs. The FE formulation based on the strain approach was initially proposed by Ashwell and Sabir [43], who developed a cylindrical shell element where the displacement field is derived by integrating assumed strain functions. This approach, as demonstrated in several subsequent studies [44–48], offers several advantages, including the straightforward satisfaction of convergence criteria, the use of independent functions for different strain components that satisfy compatibility equations, and the ability to obtain higher-order terms in the displacement field without the need for additional, nonessential degrees of freedom. The strain-based approach to plate bending has been widely applied in research, with improvements in solid FE formulations for static and dynamic analysis of thin and thick plates. Key developments include elements with reduced degrees of freedom and enhanced equilibrium conditions, enabling more efficient and accurate modeling. These elements typically use three translational degrees of freedom per node, incorporating material behavior and shear corrections for better performance in various structural analyses [49–58].

Unprecedentedly, this study represents the first attempt to evaluate both the static and buckling analysis of FGPs using a strain-based approach combined with a newly developed SSDT. While previous studies have predominantly focused on strain-based formulations within the framework of the FSDT for isotropic materials, addressing static, vibration, and buckling analyses, this work extends the application to FGPs using a higher-order theory. The novelty of this study lies in three key aspects: the development of a novel sinusoidal function that accurately captures the shear deformation effects, the application of the strain-based approach within the SSDT framework, and the combination

of these two methods to provide a more efficient and accurate analysis of FGPs. Furthermore, the study introduces a new strain-based FE, in which the sinusoidal function plays a pivotal role in reducing the number of unknowns from six to five, thereby simplifying the computational model while maintaining high accuracy. This advancement not only bridges a critical gap in the literature but also encourages further exploration of strain-based approaches for the analysis of advanced composite structures.

This article presents the static and buckling analysis of FGPs using a strain-based approach combined with a newly developed SSDT. A new higher-order strain-based FG quadrilateral plate element, denoted as HSBFGQP, is introduced to analyze the FGPs. The material properties of the FG plate vary through the thickness according to a power-law distribution of the volume fractions of its constituents. This element has five degrees of freedom (DOFs) per node, achieved by the superposition of membrane and bending elements. The membrane element, SBRIE, is the strain-based rectangular in-plane element, developed by Sabir and Sfendji [44], with two DOFs per node (u and v), while the bending element, which is the Strain based Quadrilateral Plate, denoted as SBQP, developed by Belounar et al. [54], has three DOFs (w , β_x , and β_y). To accurately capture the complex behavior of FGPs, the membrane element models the in-plane response, including normal and shear strains, while the bending element handles the plate's bending deformation. By integrating these two elements, the HSBFGQP element provides a more precise and comprehensive representation of the behavior of FGPs, effectively addressing both in-plane and bending deformations. Contrary to other HSDT formulations, which often involve more than five variables, the present approach reduces the number of unknowns to five. This is accomplished by enforcing the condition of zero transverse shear stress at both the upper and lower free surfaces of the FG plate and assuming a sinusoidal distribution of transverse shear strains through the plate's thickness. The development of this function is achieved through the comparison of shear deformation energy based on three-dimensional elasticity theory and Reissner–Mindlin theory. Additionally, the concept of potential energy is employed to formulate the stiffness and the geometric matrix. By incorporating the concept of the neutral plane, the coupling between membrane and bending behavior is effectively avoided. The results exhibit remarkable convergence with both analytical and numerical reference solutions, thereby not only validating the accuracy and reliability of the proposed approach but also demonstrating its robustness across different problem configurations. This confirms the method's efficacy in capturing the essential behavior of the system while ensuring its applicability in a wide range of scenarios, establishing it as a reliable tool for further structural analysis of FGPs.

2. Mathematical formulation

2.1. FG properties

The FG plate is composed of a mixture of ceramic and metal materials. The top surface is ceramic, and the bottom

is metal, with a continuous gradation of both materials throughout the thickness as indicated in Figure 1. The material properties are assumed to vary through the thickness of the plate following a power-law distribution as described below:

$$E(z) = (E_c - E_m)V_c + E_m, \quad (1)$$

$$V_c = \left(\frac{1}{2} + \frac{z}{h} \right)^p; \quad p \geq 0. \quad (2)$$

The expression presented includes the variable p , which indicates the exponent for the volume fraction. The values of p are assumed to be higher than or equal to zero. In addition, E denotes the young's modulus of the ceramic, whereas E_m denotes the characteristics of the metal.

At $z = \frac{h}{2}$, the modulus of elasticity $E(z)$ is equal to E_m , representing the properties of the metal. Conversely, at $z = -\frac{h}{2}$, $E(z)$ is equal to E_c , representing the properties of the ceramic. At $p=0$, the plate consists entirely of ceramic, while at p approaching infinity, the plate is composed entirely of metallic material.

2.2. Displacement field and kinematics

The displacement components vector u , v , and w in x , y , and z directions, respectively, of a point of coordinates (x, y, z) within the FG plate, are given by:

$$\begin{aligned} u(x, y, z) &= u_0(x, y) + z\beta_x(x, y) \\ v(x, y, z) &= v_0(x, y) + z\beta_y(x, y) \\ w(x, y, z) &= w_0(x, y) + f_1\psi_z(x, y) \end{aligned} \quad (3)$$

Such that: $f_1 = 2 + \cos(\frac{2\pi z}{h})$, where u_0 and v_0 are the in-plane displacement vector components at any point of the neutral plane in x and y directions, respectively. w_0 is the transverse displacement of neutral plane points of the plate and ψ_z is the stretching contributions of the displacement in the transverse direction. The variable ψ_z will be eliminated based on the assumption of zero shear stress at the top and bottom surfaces of the plate, along with the assumption that the transverse shear strains vary sinusoidally through the thickness.

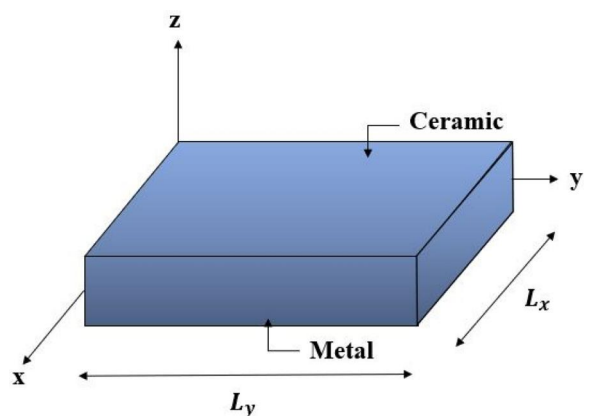


Figure 1. FG plate geometry.

Furthermore, the rotations β_x and β_y are in the yz , and xz planes, respectively.

The components of the strain vectors are derived using the nonlinear von Kármán kinematic relations. The in-plane strain vector, $\{\varepsilon\}$, is defined as the sum of the linear strain components, $\{\varepsilon^l\}$, and the nonlinear strain components, $\{\varepsilon^{nl}\}$. Additionally, the vector $\{\gamma_z^0\}$ represents the transverse shear strain:

$$\{\varepsilon\} = \{\varepsilon^l\} + \{\varepsilon^{nl}\} = \begin{Bmatrix} \varepsilon_x^l \\ \varepsilon_y^l \\ \gamma_{xy}^l \end{Bmatrix} + \begin{Bmatrix} \varepsilon_x^{nl} \\ \varepsilon_y^{nl} \\ \gamma_{xy}^{nl} \end{Bmatrix}, \quad (4)$$

$$\{\gamma_z\} = \begin{Bmatrix} \gamma_{xz} \\ \gamma_{yz} \end{Bmatrix} = \begin{Bmatrix} \gamma_{xz}^0 \\ \gamma_{yz}^0 \end{Bmatrix} + f_1 \begin{Bmatrix} \frac{\partial \psi_z}{\partial x} \\ \frac{\partial \psi_z}{\partial y} \end{Bmatrix}. \quad (5)$$

Such as:

$$\begin{aligned} \{\varepsilon^l\} &= \begin{Bmatrix} \varepsilon_x^l \\ \varepsilon_y^l \\ \gamma_{xy}^l \end{Bmatrix} = \{\varepsilon^0\} + z\{\kappa\} \\ \{\varepsilon^0\} &= \begin{Bmatrix} \varepsilon_x^0 \\ \varepsilon_y^0 \\ \gamma_{xy}^0 \end{Bmatrix} = \begin{Bmatrix} \frac{\partial u_0}{\partial x} \\ \frac{\partial v_0}{\partial x} \\ \frac{\partial u_0}{\partial y} + \frac{\partial v_0}{\partial x} \end{Bmatrix}; \{\kappa\} = \begin{Bmatrix} \kappa_x \\ \kappa_y \\ \kappa_{xy} \end{Bmatrix} = \begin{Bmatrix} \frac{\partial \beta_x}{\partial x} \\ \frac{\partial \beta_y}{\partial y} \\ \frac{\partial \beta_x}{\partial y} + \frac{\partial \beta_y}{\partial x} \end{Bmatrix}; \\ \{\varepsilon^{nl}\} &= \begin{Bmatrix} \varepsilon_x^{nl} \\ \varepsilon_y^{nl} \\ \gamma_{xy}^{nl} \end{Bmatrix} = \begin{Bmatrix} \frac{1}{2} \left(\frac{\partial w}{\partial x} \right)^2 \\ \frac{1}{2} \left(\frac{\partial w}{\partial y} \right)^2 \\ \frac{\partial w}{\partial x} \frac{\partial w}{\partial y} \end{Bmatrix}; \{\gamma_z^0\} = \begin{Bmatrix} \gamma_{xz}^0 \\ \gamma_{yz}^0 \end{Bmatrix} = \begin{Bmatrix} \beta_x + \frac{\partial w_0}{\partial x} \\ \beta_y + \frac{\partial w_0}{\partial y} \end{Bmatrix} \end{aligned} \quad (6)$$

Using Eq. (5), the variable $\psi_z(x, y)$ can be defined in term γ_{xz}^0 as follows by using the conditions of zero shear stress at the top and bottom surfaces of the plate:

$$\begin{aligned} \gamma_{xz}(x, y) &= \beta_x(x, y) + w_{0,x}(x, y) + f_1 \psi_{z,x}(x, y) \\ \gamma_{xz}\left(\pm \frac{h}{2}\right) &= \gamma_{yz}\left(\pm \frac{h}{2}\right) = 0 \text{ and } f_1\left(\pm \frac{h}{2}\right) = 1, \\ \gamma_{xz}\left(\pm \frac{h}{2}\right) &= \beta_x(x, y) + w_{0,x}(x, y) + \psi_{z,x}(x, y) \end{aligned} \quad (7)$$

which leads to:

$$\psi_{z,x}(x, y) = -\gamma_{xz}^0 \text{ and } \psi_{z,y}(x, y) = -\gamma_{yz}^0. \quad (8)$$

The shear strain components can be represented as:

$$\begin{aligned} \gamma_{xz} &= \gamma_{xz}^0(1 - f_1) \\ \gamma_{yz} &= \gamma_{yz}^0(1 - f_1) \end{aligned} \quad (9)$$

The Reissner–Mindlin theory includes correction parameters that consider the assumption that shear deformation remains constant throughout the thickness of the plate.

These parameters are determined by comparing the energy of shear deformation based on the tridimensional elasticity theory and Reissner–Mindlin theory. Hence, the shear stress for a presumed isotropic material is expressed as [20]:

$$\begin{aligned} \sigma_{xz} &= \frac{5}{6} Q_{44} \gamma_{xz}^0 \\ \sigma_{yz} &= \frac{5}{6} Q_{55} \gamma_{yz}^0. \end{aligned} \quad (10)$$

Q_{44} and Q_{55} are the materials' elasticity matrix's stiffness coefficients.

The expression of the shear strain energy per unit area is:

$$\begin{aligned} U_{sd}^{RM} &= \frac{1}{2} \int_{-\frac{h}{2}}^{\frac{h}{2}} (\sigma_{xz} \gamma_{xz}^0 + \sigma_{yz} \gamma_{yz}^0) dz \\ &= \frac{5}{12} Q_{44} h \left((\gamma_{xz}^0)^2 + (\gamma_{yz}^0)^2 \right). \end{aligned} \quad (11)$$

Additionally, the following formulas apply in the case of shear strain that varies with thickness:

$$\begin{aligned} \gamma_{xz} &= C \gamma_{xz}^0 (1 - f_1) \\ \gamma_{yz} &= C \gamma_{yz}^0 (1 - f_1), \end{aligned} \quad (12)$$

where $f(z) = C(1 - f_1) = C(-1 - \cos(\frac{2\pi z}{h}))$.

The following yields the shear stresses:

$$\tau_{xz} = Q_{44} f(z) \gamma_{xz}^0 \text{ and } \tau_{yz} = Q_{55} f(z) \gamma_{yz}^0. \quad (13)$$

The expression for the shear strain energy per unit area is as follows:

$$\begin{aligned} U_{sd}^v &= \frac{1}{2} \int_{-\frac{h}{2}}^{\frac{h}{2}} (\sigma_{xz} \gamma_{xz} + \sigma_{yz} \gamma_{yz}) dz \\ &= \frac{1}{2} Q_{44} \left((\gamma_{xz}^0)^2 + (\gamma_{yz}^0)^2 \right) C^2 \frac{3}{2} h. \end{aligned} \quad (14)$$

The two energy expressions are equalized, allowing for the following: $C^2 = \frac{5}{9}$.

Thus,

$$f(z) = \frac{-\sqrt{5}}{3} \left(1 + \cos\left(\frac{2\pi z}{h}\right) \right). \quad (15)$$

The displacement field is, therefore, defined using five unknowns, derived from the higher-order model proposed by Tati [20] as follows:

$$\begin{aligned} u(x, y, z) &= u_0(x, y) + z\beta_x(x, y) \\ v(x, y, z) &= v_0(x, y) + z\beta_y(x, y) \\ w(x, y, z) &= f(z)w_0(x, y) + (f(z) - 1)G(x, y) \end{aligned}, \quad (16)$$

where the function $G(x, y)$ is defined by:

$$\beta_x = \frac{\partial G(x, y)}{\partial x}; \beta_y = \frac{\partial G(x, y)}{\partial y}.$$

The components of the shear strain vector and the nonlinear strain vector become:

$$\{\gamma_z\} = f(z)\{\gamma_z^0\} = f(z) \begin{Bmatrix} \gamma_{xz}^0 \\ \gamma_{yz}^0 \end{Bmatrix}, \quad (17)$$

$$\begin{aligned} \{\varepsilon^{nl}\} &= \begin{Bmatrix} \varepsilon_x^{nl} \\ \varepsilon_y^{nl} \\ \gamma_{xy}^{nl} \end{Bmatrix} = \begin{Bmatrix} \frac{1}{2} \left(\frac{\partial w}{\partial x} \right)^2 \\ \frac{1}{2} \left(\frac{\partial w}{\partial y} \right)^2 \\ \frac{\partial w}{\partial x} \frac{\partial w}{\partial y} \end{Bmatrix} \\ &= \frac{1}{2} \begin{Bmatrix} \left(f(z) \frac{\partial w_0}{\partial x} + (fz) - 1 \right) \beta_x^2 \\ \left(f(z) \frac{\partial w_0}{\partial y} + (fz) - 1 \right) \beta_y^2 \\ 2 \left(f(z) \frac{\partial w_0}{\partial x} + (fz) - 1 \right) \beta_x \left(f(z) \frac{\partial w_0}{\partial y} + (fz) - 1 \right) \beta_y \end{Bmatrix}. \end{aligned} \quad (18)$$

2.3. Constitutive equations

The stress-strain relationship for an elastic FG plate is defined as:

$$\begin{Bmatrix} \sigma_x \\ \sigma_y \\ \tau_{xy} \\ \tau_{xz} \\ \tau_{yz} \end{Bmatrix} = \begin{bmatrix} S_{11} & S_{12} & 0 & 0 & 0 \\ S_{21} & S_{22} & 0 & 0 & 0 \\ 0 & 0 & S_{66} & 0 & 0 \\ 0 & 0 & 0 & S_{55} & 0 \\ 0 & 0 & 0 & 0 & S_{44} \end{bmatrix} \begin{Bmatrix} \varepsilon_x^l \\ \varepsilon_y^l \\ \gamma_{xy}^l \\ \gamma_{xz} \\ \gamma_{yz} \end{Bmatrix}. \quad (19)$$

Based on Eq. (1), the stiffness coefficients S_{ij} are as follows:

$$\begin{aligned} S_{11} = S_{22} &= \frac{E(z)}{1 - \nu^2}, \quad S_{12} = S_{21} = \frac{\nu E(z)}{1 - \nu^2}, \\ S_{44} = S_{55} = S_{66} &= \frac{E(z)}{2(1 + \nu)}. \end{aligned}$$

So, the stresses and the strains matrix are:

$$\begin{aligned} \{\sigma\} &= \{\sigma_x \ \sigma_y \ \tau_{xy}\}^T; \quad \{\tau_z\} = \{\tau_{xz} \ \tau_{yz}\}^T, \\ \{\gamma_z\} &= \{\gamma_{xz} \ \gamma_{yz}\}^T; \quad \{\varepsilon\} = \{\varepsilon_x \ \varepsilon_y \ \gamma_{xy}\}^T. \end{aligned} \quad (20)$$

3. Forces and moments resulting

Departing from the mid-plane of the plate, the forces and moments are obtained with respect to the neutral plane, as seen in Figure 2. This prevents the bending and membrane behaviors caused by the asymmetry in the thickness of the plate from interacting with one another. The position of the physical neutral plane is determined by the condition that the in-plane force resulting from bending at the neutral plane is equal to zero [59,60]:

$$\begin{aligned} e &= \frac{\int_{-\frac{h}{2}}^{\frac{h}{2}} E(z) z dz}{\int_{-\frac{h}{2}}^{\frac{h}{2}} E(z) dz}, \\ z_{Np} &= z - e \end{aligned} \quad (21)$$

Given the stress components through the thickness, the forces and moments per unit length are given by:

$$\begin{aligned} \begin{Bmatrix} N_x \\ N_y \\ N_{xy} \end{Bmatrix} &= \int_{-\frac{h}{2}}^{\frac{h}{2}} \begin{Bmatrix} \sigma_x \\ \sigma_y \\ \tau_{xy} \end{Bmatrix} dz; \quad \begin{Bmatrix} M \\ M_y \\ M_{xy} \end{Bmatrix} = \int_{-\frac{h}{2}}^{\frac{h}{2}} \begin{Bmatrix} \sigma_x \\ \sigma_y \\ \tau_{xy} \end{Bmatrix} (z - e) dz; \\ \begin{Bmatrix} T_x \\ T_y \end{Bmatrix} &= \int_{-\frac{h}{2}}^{\frac{h}{2}} \begin{Bmatrix} \tau_{xz} \\ \tau_{yz} \end{Bmatrix} dz. \end{aligned} \quad (22)$$

The stress resultants and strains can be expressed in matrix form as follows:

$$\begin{Bmatrix} N \\ M \\ T \end{Bmatrix} = \begin{bmatrix} [A] & 0 & 0 \\ 0 & [D] & 0 \\ 0 & 0 & [A_s] \end{bmatrix} \begin{Bmatrix} \varepsilon^0 \\ \kappa \\ \gamma_z \end{Bmatrix}. \quad (23)$$

The reduced matrices $[A]$, $[D]$, and $[A_s]$ can be expressed in the context of the neutral plane as follows:

$$\begin{aligned} [A] &= \begin{bmatrix} 1 & \nu & 0 \\ \nu & 1 & 0 \\ 0 & 0 & \frac{1-\nu}{2} \end{bmatrix} \int_{-\frac{h}{2}}^{\frac{h}{2}} \frac{E(z)}{(1-\nu^2)} dz \\ [D] &= \begin{bmatrix} 1 & \nu & 0 \\ \nu & 1 & 0 \\ 0 & 0 & \frac{1-\nu}{2} \end{bmatrix} \int_{-\frac{h}{2}}^{\frac{h}{2}} \frac{E(z)}{(1-\nu^2)} (z - e)^2 dz. \\ [A_s] &= \begin{bmatrix} 1 & 0 \\ 0 & 1 \end{bmatrix} \int_{-\frac{h}{2}}^{\frac{h}{2}} \frac{E(z)}{2(1+\nu)} (f(z))^2 dz \end{aligned} \quad (24)$$

4. Formulation of the developed element using the FEM

The present element denoted as HSBFGQP is a four-node quadrilateral FG element. Each node has five degrees of freedom, as shown in Figure 3. These include three translations (u , v , w) in the x , y , and z directions, and two rotations (β_x and β_y) in the x , and y planes. Therefore, each element has a total of 20 degrees of freedom.

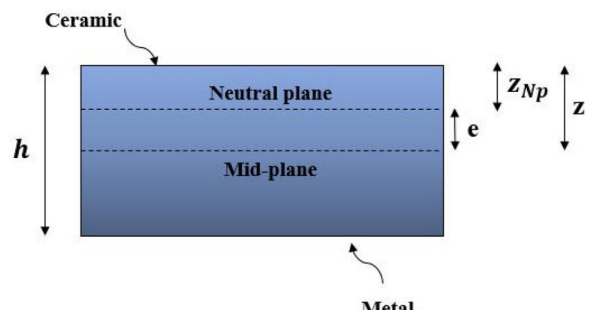


Figure 2. Location of the neutral plane in FG plate.

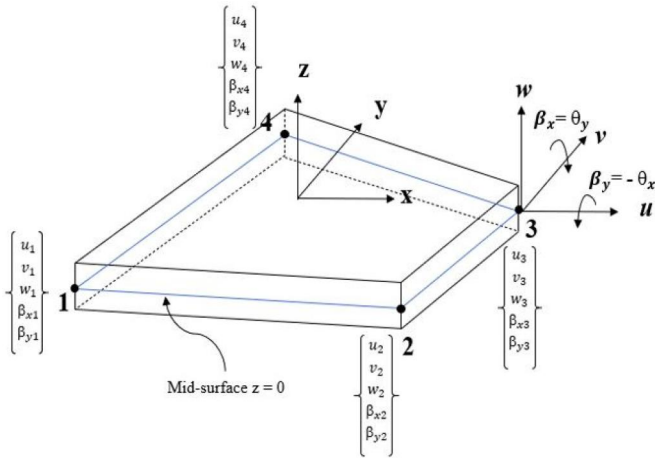


Figure 3. The HSBFGQP geometry.

4.1. The element's displacement interpolation

The displacement fields obtained from the membrane element (SBRIE) [44], and the plate element (SBQP) [54] are examined to develop the displacement functions of the current element.

As stated in Ref. [44], the membrane element's displacement field is as follows:

$$\begin{Bmatrix} u \\ v \end{Bmatrix} = [P_m]_{2 \times 8} \{\alpha_m\}. \quad (25)$$

Such that: $\{\alpha_m\}$ is the membrane's vector of constant parameters,

$$\{\alpha_m\} = \{\alpha_{m1}, \alpha_{m2}, \dots, \alpha_{m8}\}^T.$$

The matrix $[P_m]$ is defined as follows:

$$[P_m] = \begin{bmatrix} 1 & 0 & -y & x & xy & 0 & \frac{-y^2}{2} & \frac{y}{2} \\ 0 & 1 & x & 0 & \frac{-x^2}{2} & y & xy & \frac{x}{2} \end{bmatrix}. \quad (26)$$

The bending element's displacement field is provided by Belounar et al. [54]:

$$\begin{Bmatrix} w \\ \beta_x \\ \beta_y \end{Bmatrix} = [P_b]_{3 \times 12} \{\alpha_b\}. \quad (27)$$

Such that: $\{\alpha_b\}$ is the bending's vector of constant parameters; $\{\alpha_b\} = \{\alpha_{b9}, \alpha_{b14}, \dots, \alpha_{b20}\}^T$

The matrix $[P_b]$ is defined as follows:

$$(P_b) = \begin{bmatrix} 0 & 0 & 0 & 0 & 0 & 0 & 0 & 0 & 1 & -x & -y \\ 0 & 0 & 0 & 0 & 0 & 0 & 0 & 0 & 0 & 1 & 0 \\ 0 & 0 & 0 & 0 & 0 & 0 & 0 & 0 & 0 & 0 & 1 \end{bmatrix} \begin{bmatrix} \frac{-x^2}{2} & \frac{-x^2y}{2} & \frac{-y^2}{2} & \frac{-xy^2}{2} & \frac{-xy}{2} & \frac{x}{2} & \frac{xy}{2} & \frac{y}{2} & \frac{xy}{2} \\ x & xy & 0 & \frac{y^2}{2} & \frac{y}{2} & \frac{1}{2} & \frac{y}{2} & 0 & \frac{y}{2} \\ 0 & \frac{x^2}{2} & y & xy & \frac{x}{2} & 0 & \frac{-x}{2} & \frac{1}{2} & \frac{x}{2} \end{bmatrix}. \quad (28)$$

Equations (25) and (27) can be superposed to yield the interpolation functions of the displacement for the evolved element HSBFGQP, as previously stated.

$$\{U_e\} = \begin{Bmatrix} u \\ v \\ w \\ \beta_x \\ \beta_y \end{Bmatrix} = \begin{bmatrix} [P_m] & 0 \\ 0 & [P_b] \end{bmatrix}_{5 \times 20} \begin{Bmatrix} \{\alpha_m\} \\ \{\alpha_b\} \end{Bmatrix} = [P]\{\alpha\}, \quad (29)$$

where $\{\alpha\} = \{\alpha_1, \alpha_2, \dots, \alpha_{20}\}^T$

$$[P] = \begin{bmatrix} [P_m] & [0]_{2 \times 12} \\ [0]_{3 \times 8} & [P_b] \end{bmatrix}. \quad (30)$$

The transformation matrix $[C]$ relates the 20 constants $\{\alpha\}$ to the 20 degrees of freedom of the element, as described below:

$$\{q_e\} = [C]\{\alpha\}, \quad (31)$$

where $[C]_{20 \times 20} = [[P_1][P_2][P_3][P_4]]^T$.

In addition, the matrix $[P]_i$ is constructed for each node using Eq. (30). This results in:

$$[P]_i = \begin{bmatrix} [P_m]_i & 0 \\ 0 & [P_b]_i \end{bmatrix}_{i=1,4}. \quad (32)$$

Equation (31) allows to get the vector of constant parameters:

$$\{\alpha\} = [C]^{-1}\{q_e\}. \quad (33)$$

Substituting Eq. (33) into Eq. (29) yields:

$$\{U_e\} = [P][C]^{-1}\{q_e\} = [N]\{q_e\}, \quad (34)$$

where

$$[N] = [P][C]^{-1}. \quad (35)$$

This interpolation is crucial for analyzing strain matrices and deriving the load vector of the element.

4.2. Analysis of the strain matrices

The strains associated with membrane behavior are expressed in terms of displacements in the following manner:

$$\left\{ \begin{matrix} \varepsilon_x^0 \\ \varepsilon_y^0 \\ \gamma_{xy}^0 \end{matrix} \right\} = \left[\begin{matrix} \frac{\partial}{\partial x} & 0 \\ 0 & \frac{\partial}{\partial y} \\ \frac{\partial}{\partial y} & \frac{\partial}{\partial x} \end{matrix} \right] \left\{ \begin{matrix} u \\ v \end{matrix} \right\}. \quad (36)$$

Replacing Eq. (29) with Eq. (36) yields:

$$\{\varepsilon^0\} = \begin{bmatrix} \frac{\partial}{\partial x} & 0 \\ 0 & \frac{\partial}{\partial y} \\ \frac{\partial}{\partial y} & \frac{\partial}{\partial x} \end{bmatrix} \begin{bmatrix} [P_m] & [0] \end{bmatrix}_{3 \times 20} \{\alpha_m\} = [Q_m]\{\alpha_m\}. \quad (37)$$

The membrane strains matrix $[Q_m]$ is as follows:

Following are the curvatures-displacements relations:

$$\begin{aligned} \{\kappa\} &= \begin{Bmatrix} \kappa_x \\ \kappa_y \\ \kappa_{xy} \end{Bmatrix} = \begin{bmatrix} 0 & \frac{\partial}{\partial x} & 0 \\ 0 & 0 & \frac{\partial}{\partial y} \\ 0 & \frac{\partial}{\partial y} & \frac{\partial}{\partial x} \end{bmatrix} \begin{Bmatrix} w \\ \beta_x \\ \beta_y \end{Bmatrix} . \\ \{\gamma_z^0\} &= \begin{Bmatrix} \gamma_{xz}^0 \\ \gamma_{yz}^0 \end{Bmatrix} = \begin{bmatrix} \frac{\partial}{\partial x} & 1 & 0 \\ \frac{\partial}{\partial y} & 0 & 1 \end{bmatrix} \begin{Bmatrix} w \\ \beta_x \\ \beta_y \end{Bmatrix} \end{aligned} \quad (39)$$

Substituting Eq. (29) into Eq. (39) yields:

$$\begin{aligned} \{\kappa\} &= \begin{Bmatrix} \kappa_x \\ \kappa_y \\ \kappa_{xy} \end{Bmatrix} = \begin{bmatrix} 0 & \frac{\partial}{\partial x} & 0 \\ 0 & 0 & \frac{\partial}{\partial y} \\ 0 & \frac{\partial}{\partial y} & \frac{\partial}{\partial x} \end{bmatrix} \begin{bmatrix} [0] & [P_b] \end{bmatrix}_{3 \times 20} \{\alpha_b\} = [Q_b] \{\alpha_b\} \\ \{\gamma_z^0\} &= \begin{bmatrix} \frac{\partial}{\partial x} & 1 & 0 \\ \frac{\partial}{\partial y} & 0 & 1 \end{bmatrix} \begin{bmatrix} [0] & [P_b] \end{bmatrix}_{2 \times 20} \{\alpha_b\} = [Q_s] \{\alpha_b\} \end{aligned} \quad . \quad (40)$$

In which $[Q_b]$ and $[Q_s]$, respectively, are:

$$[Q_b] = \begin{bmatrix} 0 & 0 & 0 & 0 & 0 & 0 & 0 & 0 & 0 & 0 & 0 & 1 & y & 0 & 0 & 0 & 0 & 0 & 0 & 0 \\ 0 & 0 & 0 & 0 & 0 & 0 & 0 & 0 & 0 & 0 & 0 & 0 & 1 & x & 0 & 0 & 0 & 0 & 0 & 0 \\ 0 & 0 & 0 & 0 & 0 & 0 & 0 & 0 & 0 & 0 & 0 & 2x & 0 & 2y & 1 & 0 & 0 & 0 & 0 & 0 \end{bmatrix}, \quad (41)$$

The geometric strains are formulated as follows:

$$\{\varepsilon^g\} = \begin{Bmatrix} \frac{\partial w}{\partial x} \\ \frac{\partial w}{\partial y} \end{Bmatrix} = [R]_{2 \times 20} \{\alpha_b\}, \quad (43)$$

where the matrix $[R]$ is:

$$[R] = \begin{bmatrix} 0 & 0 & 0 & 0 & 0 & 0 & 0 & 0 & -1 & 0 & -x & -xy & 0 & \frac{-y^2}{2} & \frac{-y}{2} & \frac{1}{2} & \frac{y}{2} & 0 & \frac{y}{2} \\ 0 & 0 & 0 & 0 & 0 & 0 & 0 & 0 & 0 & -1 & 0 & \frac{-x^2}{2} & -y & -xy & \frac{-x}{2} & 0 & \frac{x}{2} & \frac{1}{2} & \frac{x}{2} \end{bmatrix}. \quad (44)$$

The relationships between the strains and the element nodal displacements can be obtained by substituting Eq. (33) into Eqs. (37), (40), and (43):

$$\begin{aligned} \{\varepsilon^0\} &= [Q_m][C]^{-1}\{q_e\} = [B_m]\{q_e\} \\ \{\kappa\} &= [Q_b][C]^{-1}\{q_e\} = [B_b]\{q_e\} \\ \{\gamma_z^0\} &= [Q_s][C]^{-1}\{q_e\} = [B_s]\{q_e\} \\ \{\varepsilon^g\} &= [R][C]^{-1}\{q_e\} = [B_g]\{q_e\} \end{aligned} . \quad (45)$$

The membrane, bending, shear, and geometric strain matrices $[B_m]$, $[B_b]$, $[B_s]$, and $[B_g]$, respectively, are defined as follows:

$$[B_m] = [Q_m][C]^{-1}; [B_b] = [Q_b][C]^{-1}; [B_s] = [Q_s][C]^{-1}; [B_g] = [R][C]^{-1}. \quad (46)$$

4.3. Elementary stiffness matrices' derivation

4.3.1. Static analysis

The element's elementary stiffness matrix has been derived using the total potential energy principle.

Regarding the neutral plane z_{NP} , the potential energy of deformation and the work done by external forces are represented by E_{pd} and W_{ext} , respectively. The potential energy of the FG plate is expressed as follows:

$$E_p = E_{pd} - W_{ext}, \quad (47)$$

$$E_{pd} = \frac{1}{2} \int (\{\varepsilon^l\}^T \{\sigma\} + \{\gamma_z\}^T \{\tau_z\}) dV. \quad (48)$$

Integrating throughout the thickness of the plate [20]:

$$E_{pd} = \frac{1}{2} \int \left((\{\varepsilon^0\}^T [A] \{\varepsilon^0\} + \{\kappa\}^T [D] \{\kappa\} + \{\gamma_z^0\}^T [A_s] \{\gamma_z^0\}) \right) d\Omega. \quad (49)$$

V and Ω represent the volume and top surface of the plate, respectively.

The external work performed by the distributed transverse load $q(x, y)$ applied to the FG plate can be expressed as [20,23]:

$$W_{ext} = \int_{\Omega} w(x, y) q(x, y) d\Omega. \quad (50)$$

Substituting Eq. (29) into Eq. (50) yields:

$$W_{ext} = \int_{\Omega} \{q_e\}^T [N]^T \{q(x, y)\} d\Omega. \quad (51)$$

Using Eqs. (49) and (51), the following can be used to express the total potential energy of the previous expression:

$$E_p = \frac{1}{2} \int_{\Omega} \left(\{q_e\}^T ([B_m]^T [A] [B_m] + [B_b]^T [D] [B_b] + [B_s]^T [A_s] [B_s]) \{q_e\} \right) d\Omega - \int_{\Omega} \{q_e\}^T [N]^T \{q(x, y)\} d\Omega. \quad (52)$$

The equation of equilibrium for linear bending behavior can be expressed as follows, with $[K_e]$ representing the element stiffness matrix and $\{F_e\}$ denoting the element nodal forces vector, are defined below:

$$[K_e] \{q_e\} = \{F_e\}, \quad (53)$$

$$[K_e] = \int_{\Omega} \left([B_m]^T [A] [B_m] + [B_b]^T [D] [B_b] + [B_s]^T [A_s] [B_s] \right) d\Omega. \quad (54)$$

The formula of the stiffness matrix become:

$$[K_e] = [K_e^m] + [K_e^b] + [K_e^s]. \quad (55)$$

Such that $[K_e^m]$ present the element membrane stiffness matrix, $[K_e^b]$ present the element bending stiffness, and $[K_e^s]$ is the element shear stiffness matrix, their formulas are as follows:

$$\begin{aligned} [K_e^m] &= \int_{\Omega} ([B_m]^T [A] [B_m]) d\Omega = [C]^{-T} \left(\int_{-b-a}^b \int_{-a}^a [Q_m]^T [A] [Q_m] dx dy \right) [C]^{-1} \\ [K_e^b] &= \int_{\Omega} ([B_b]^T [D] [B_b]) d\Omega = [C]^{-T} \left(\int_{-b-a}^b \int_{-a}^a [Q_b]^T [D] [Q_b] dx dy \right) [C]^{-1}, \\ [K_e^s] &= \int_{\Omega} ([B_s]^T [A_s] [B_s]) d\Omega = [C]^{-T} \left(\int_{-b-a}^b \int_{-a}^a [Q_s]^T [A_s] [Q_s] dx dy \right) [C]^{-1} \end{aligned} \quad (56)$$

$$\{F_e\} = \int_{\Omega} [N]^T \{q(x, y)\} d\Omega. \quad (57)$$

4.3.2. Buckling analysis

The external work caused by in-plane forces due to mechanical loading can be expressed as [21,22]:

$$W_{ext} = \int_{\Omega} \{\epsilon^{nl}\}^T [N] d\Omega. \quad (58)$$

The subsequent equation is obtained through replacement Eqs. (49) and (58) into Eq. (47):

$$\begin{aligned} E_p &= \frac{1}{2} \int_{-b}^b \int_{-a}^a \left(\{\epsilon^0\}^T \{N\} + \{\kappa\}^T \{M\} + \{\gamma_z\}^T \{T\} \right) dx dy \\ &\quad - \frac{1}{2} \int_{-b}^b \int_{-a}^a \left(\{\epsilon^{nl}\}^T \{N\} \right) dx dy, \end{aligned} \quad (59)$$

$$\begin{aligned} E_p &= \frac{1}{2} \int_{-b}^b \int_{-a}^a \{q_e\}^T \left([B_m]^T [A] [B_m] + [B_b]^T [D] [B_b] + [B_s]^T [A_s] [B_s] \right) \{q\} dx dy \\ &\quad - \frac{1}{2} \int_{-b}^b \int_{-a}^a \{q_e\}^T \left([R]^T [\dot{N}]^T [R] \right) \{q_e\} dx dy. \end{aligned} \quad (60)$$

$[\dot{N}] = \begin{bmatrix} \beta_1 & \beta_{12} \\ \beta_{21} & \beta_2 \end{bmatrix}$ is the mechanical loading-induced stress matrix.

Eliminating the second variation of total potential energy for nodal values $\{q\}$ reveals the eigenvalue issue in Refs. [21,22]:

$$([K_e] + [K_g^e]) \{q\} = 0. \quad (61)$$

$[K_g^e]$ is the geometric stiffness matrix; it is provided by:

$$[K_g^e] = \int_{-b}^b \int_{-a}^a [R]^T [\dot{N}] [R] dx dy. \quad (62)$$

The loading factor λ allows for the expression of the stress matrix to be $[\dot{N}] = \lambda [\dot{N}_0]$, where $[\dot{N}_0]$ is the stress matrix as a result of the mechanical load N_0 provided; thus, the geometric stiffness matrix has the following form:

$$[K_g^e] = \int_{-\frac{h}{2}}^{\frac{h}{2}} \int_{-b}^b \int_{-a}^a [R]^T [\dot{N}_0] [R] dx dy dz. \quad (63)$$

The matrices $[K_e]$, $[K_g^e]$ and the element nodal equivalent load vector $\{F_e\}$, as indicated in Eqs. (55), (63), and (57) correspondingly, are calculated numerically. The structural load vector $\{F\}$, along with the structural stiffness and geometric stiffness matrices ($[K]$, $[K_g^e]$), is derived by assembling these matrices and vectors.

The critical buckling load $N_{cr} = \lambda_{cr} N_0$, finally, can be determined by solving the following eigenvalue problem:

$$\det([K] + \lambda [K_g^e]) = 0. \quad (64)$$

5. Numerical result and discussion

This study provides an investigation of the FGPs, specifically composed from aluminum (Al) and alumina (Al_2O_3). The attributes and mechanical qualities of these plates are:

- Top surface: ceramic (Al_2O_3), $E_c = 380$ GPa; $\nu_c = 0.3$
- Bottom surface: metal (Al), $E_m = 70$ GPa; $\nu_m = 0.3$

Different mesh sizes, ranging from 8×8 to 24×24 aspects, are employed for convergence study on square FG plate, where L_x and L_y denote the length and width of the plate, respectively, as illustrated in Figures 3 and 4.

The selection of square and rectangular FGPs for the study of static and buckling behaviors is motivated by their

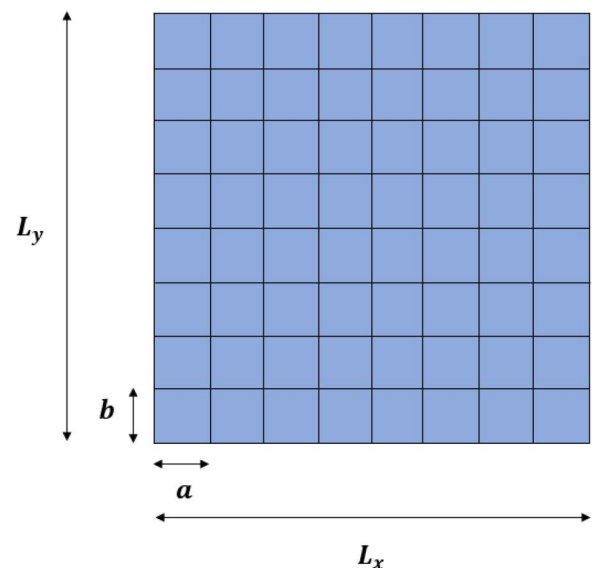


Figure 4. Mesh configuration for the FG plate.

practical applications in engineering structures. Square plates serve as a fundamental geometry for benchmarking and validation due to their symmetry and uniformity, while rectangular plates are commonly encountered in aerospace, naval, and architectural applications where elongated geometries are required. These two configurations enable a comprehensive analysis of the influence of material gradation, BCs, and geometric parameters on the mechanical performance of FGPs. This study examines several BCs, represented by four letters denoting the behavior of the plate's four edges as noted in **Table 1**. For instance, SCSC denotes that the plate edges are simply supported-clamped, starting at the right edge in a counter clockwise direction. The value 1 is used to represent a constrained DOF, meaning that the displacement or rotation is restricted. Conversely, the value 0 indicates a free DOF, meaning that no constraints are applied to the displacement or rotation. This notation is used to describe the BCs applied in the analysis.

The selected BCs for this study represent various real-world scenarios. These configurations simulate a range of practical applications, such as rigidly fixed structures, framed floors, cantilevered plates, and plates embedded or supported in different ways, allowing for a comprehensive analysis of bending, buckling, and dynamic behaviors.

A convergence study for the static and buckling behavior is initially conducted to validate the accuracy and reliability of the proposed algorithm. The results, derived from multiple mesh configurations, are compared with the well-established and widely recognized reference solutions provided by Zenkour [15,24].

Then, a static analysis is conducted to determine the displacement and stresses of the FG plate with a varying side-to-thickness ratio, different values of the power-law index p , BCs, and plate's geometry. As indicated in **Figure 5**, the plate was subjected to a uniformly distributed load (UDL), with the load formulas as follows:

$$q(x,y) = q_0. \quad (67)$$

The outcomes derived from the present formulation, regarding deflections and stresses, are compared with those from existing literature and expressed in terms of nondimensional central deflections and stresses defined by the examples that follows. The formulas are as detailed below:

Table 1. Boundary conditions and associated displacement constraints.

BCs	Denotation	Edge definition	u	v	w	β_x	β_y
CCCC	Fully clamped	$x=0; L_x$	1	1	1	1	1
		$y=0; L_y$	1	1	1	1	1
SSSS	Fully simply supported	$x=0; L_x$	0	1	1	0	1
		$y=0; L_y$	1	0	1	1	0
SCSC	Simply clamped	$x=0; L_x$	1	1	1	1	1
		$y=0; L_y$	1	0	1	1	0
SFSC	Simply free-simply-clamped	$x=0$	1	1	1	1	1
		$y=0; L_y$	1	0	1	1	0
SFSS	Simply free-simply	$x=0$	0	1	1	0	1
		$y=0; L_y$	1	0	1	1	0
SSSC	Simply supported-clamped	$x=0$	1	1	1	1	1
		$x=L_x$	0	1	1	0	1
		$y=0; L_y$	1	0	1	1	0

$$\begin{aligned} \bar{w} &= \frac{10h^3E_c}{q_0L^4} w\left(\frac{L_x}{2}, \frac{L_y}{2}\right); \bar{\sigma}_x &= \frac{h}{q_0L} \sigma_x\left(\frac{L_x}{2}, \frac{L_y}{2}, \frac{h}{2}\right); \bar{\sigma}_y &= \frac{h}{q_0L} \sigma_y\left(\frac{L_x}{2}, \frac{L_y}{2}, \frac{h}{3}\right); \\ \bar{\tau}_{xy} &= \frac{h}{q_0L} \tau_{xy}\left(0, 0, -\frac{h}{3}\right); \bar{\tau}_{xz} &= \frac{h}{q_0L} \tau_{xz}\left(0, \frac{L_y}{2}, 0\right); \bar{\tau}_{yz} &= \frac{h}{q_0L} \tau_{yz}\left(\frac{L_x}{2}, 0, \frac{h}{6}\right). \end{aligned} \quad (68)$$

The choice of UDL is justified as it represents common practical scenarios often encountered in engineering applications, such as concrete slabs and plates. This loading condition allows for the comprehensive assessment of flexural resistance, deformation, and structural performance of FGPs under static loading, providing results that are directly applicable to real-world design and analysis.

Finally, the buckling behavior of FGPs is investigated. A parametric analysis is conducted to analyze the effect of the power-law index p , side-to-thickness ratio, uniaxial and biaxial compression, aspect ratio, and BCs.

Uniaxial and biaxial compression are essential for FGPs as they replicate real-world loading scenarios commonly encountered in engineering applications. Uniaxial compression examines the plate's response to directional compressive stresses, typical in structures like beams or columns. Biaxial compression, conversely, provides critical insights into the behavior of FGPs under multi-axial stress states, as seen in slabs, pressure vessels, and aerospace structures. These loading conditions allow for a thorough assessment of the mechanical stability, buckling resistance, and structural performance of FGPs in practical applications.

The dimensionless critical buckling load is presented using the following formula:

$$\bar{N}_{cr} = \frac{N_{cr}L_x^2}{E_m h^3}. \quad (69)$$

5.1. Convergence study

To assess the impact of mesh refinement on the accuracy of the results for both bending and buckling behaviors of the plate, a convergence analysis of an SSSS square Al/Al₂O₃ plate subjected to UDL, with side-to-thickness ratios $L_x/h = 10$ is presented in this subsection. The study investigates the behavior of the plate under different mesh sizes, ranging from 4×4 to 24×24 , and for various power-law index p .

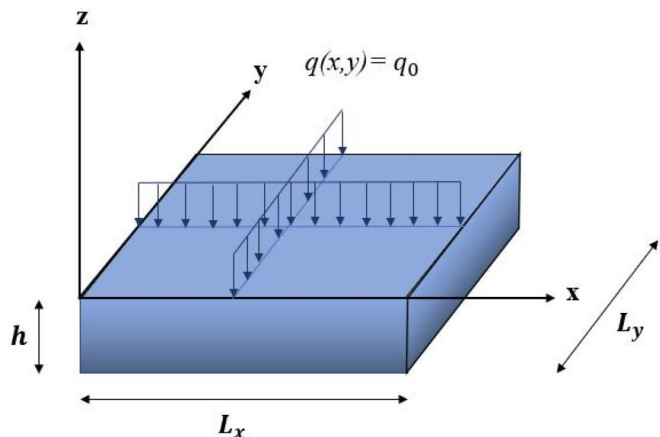


Figure 5. Distribution of the UDL on the FG plate.

First, a convergence study is performed for the static behavior. Table 2 presents the nondimensional central deflection of the SSSS FG plate for various mesh sizes and power-law index p . The results demonstrate that the proposed element converges effectively as the mesh becomes finer. For instance, for $p=0$, the deflection stabilizes at 0.4660 with a 24×24 mesh, closely matching the reference value of 0.4665 provided by Zenkour [15]. Similarly, for other values of p , the results approach those of Zenkour, with slight discrepancies that decrease as the mesh size increases. This confirms the accuracy and reliability of the proposed element, particularly when compared to Zenkour's well-established and widely cited results.

Figure 6, which represents the bending relative errors, further illustrates the convergence behavior. For all power-law indices p , the relative errors decrease significantly as the mesh size increases. With a coarse 4×4 mesh, the relative error reaches approximately 4.5% in some cases. However, with an 8×8 mesh, the error drops below 1.5%, and it further decreases to less than 1% for a 12×12 mesh. Beyond 16×16 , the errors stabilize around 0.5%, while finer meshes such as 20×20 and 24×24 provide even higher accuracy, with discrepancies below 0.2%. The 20×20 mesh already delivers reliable results comparable to the 24×24 mesh, though the latter offers slightly better accuracy. For higher values of p , specifically $p=5$ and $p=10$, the relative errors exhibit greater divergence, especially for coarser meshes. This can be attributed to the increased sensitivity of the

Table 2. Convergence of the nondimensional central deflection of SSSS FG plate under UDL ($L_x/h = 10$).

p	4×4	8×8	12×12	16×16	20×20	24×24	Zenkour [15]
0	0.4454	0.4616	0.4644	0.4654	0.4658	0.4660	0.4665
1	0.8859	0.9187	0.9244	0.9263	0.9272	0.9277	0.9287
2	1.1428	1.1845	1.1917	1.1942	1.1953	1.1959	1.1940
5	1.3847	1.4329	1.4411	1.4440	1.4453	1.4460	1.4356
10	1.5321	1.5845	1.5935	1.5966	1.5980	1.5988	1.5876

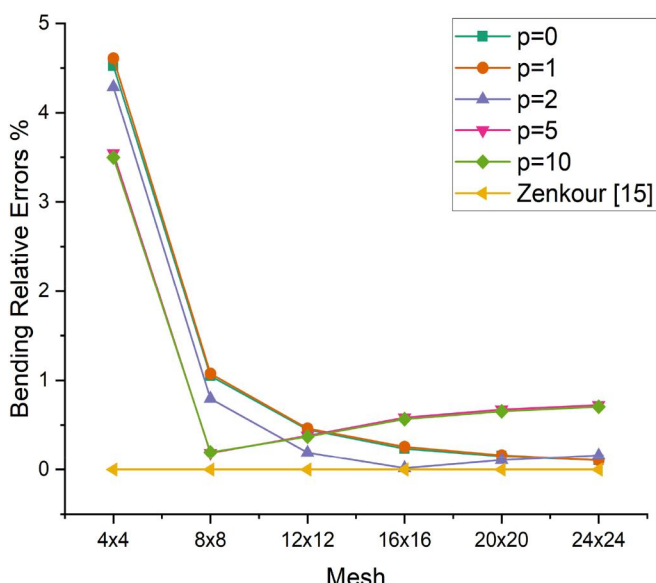


Figure 6. Relative errors in the nondimensional central deflections for various mesh densities and power law index.

system to both shear effects and material property gradients as p increases.

Based on these results, the choice of the 24×24 mesh is further justified as it captures the FG plate's behavior with high accuracy while minimizing relative errors. The convergence stabilizes at this mesh size for all p , with deviations below 0.1% compared to Zenkour's values. This ensures reliable results without unnecessary computational cost, making the 24×24 mesh an optimal balance between accuracy and efficiency.

Next, a convergence study of the mesh for the buckling analysis is performed. The nondimensional critical buckling loads of the FG plate for various mesh sizes and power-law indices p are presented in Table 3. The results indicate that the proposed element demonstrates excellent convergence behavior as the mesh is refined. For instance, for $p=0$, the critical buckling load stabilizes at 18.5593 with a 24×24 mesh, which is very close to the reference value of 18.5785 provided by Zenkour and Aljadani [61]. Similarly, for higher values of p , the critical buckling loads approach Zenkour's values, with discrepancies decreasing as the mesh becomes finer. The 12×12 and 16×16 meshes already provide a reasonable approximation of the buckling loads, with errors significantly reduced compared to coarser meshes such as 4×4 and 8×8 . However, for 20×20 and 24×24 meshes, the results become nearly indistinguishable from Zenkour's reference values, highlighting the high accuracy of the proposed model.

Figure 7, which presents the relative errors of the buckling analysis, clearly illustrates the improvement in convergence behavior as the mesh size increases. For a coarse 4×4 mesh, the relative error reaches approximately 4% in some cases. However, with an 8×8 mesh, the errors drop significantly, ranging between 1.5% and 2.5%, depending on the power-law index. From a 12×12 mesh onward, the errors continue to decrease, reaching values between 1% and 1.5%. As the mesh size reaches 16×16 , the errors stabilize between 0.5% and 1%, while a 20×20 mesh further reduces them to approximately 0.3–0.7%. Finally, with a 24×24 mesh, the errors remain slightly below 0.5%, offering a marginal improvement compared to the 20×20 mesh, indicating that further mesh refinement beyond this point yields diminishing returns.

It can be concluded that the 20×20 mesh provides sufficiently accurate results for the buckling analysis, closely matching Zenkour's values with very small errors. Since no significant improvements are observed with the 24×24 mesh, and additional computational resources are required, the 20×20 mesh is considered the most suitable choice for balancing accuracy and computational efficiency.

Table 3. Convergence of the nondimensional critical buckling load of SSSS FG plate ($L_x/h = 10$).

p	4×4	8×8	12×12	16×16	20×20	24×24	Zenkour and Aljadani [61]
0	17.9510	18.4123	18.5036	18.5360	18.5511	18.5593	18.5785
1	9.0177	9.2539	9.3007	9.3173	9.3250	9.3292	9.3391
2	6.9953	7.1759	7.2116	7.2243	7.2302	7.2334	7.2630
5	5.7856	5.9271	5.9550	5.9650	5.9696	5.9721	6.0353
10	5.2328	5.3585	5.3833	5.3921	5.3962	5.3985	5.4528

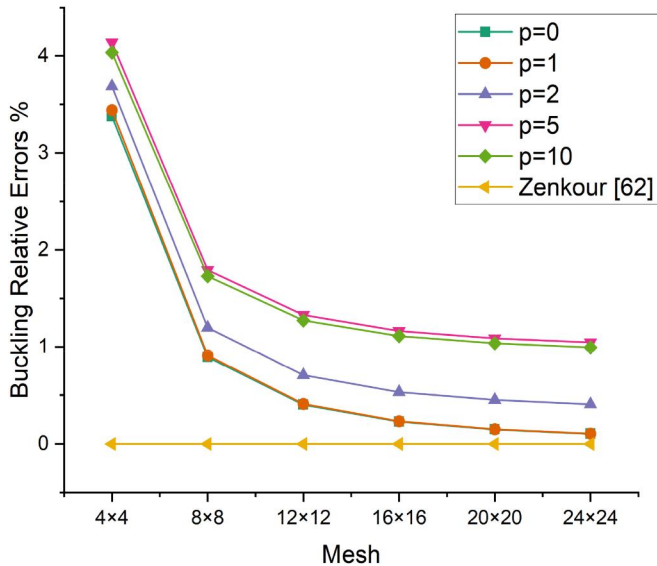


Figure 7. Relative errors in nondimensional critical buckling load for various mesh sizes and power law index p .

Table 4. Side to thickness ratio's impact on a FG square plate's stresses and nondimensional displacements ($p = 0$) under UDL.

$\frac{L_x}{h}$	Theory	\bar{w}	$\bar{\sigma}_x$	$\bar{\sigma}_y$	$\bar{\tau}_{xy}$	$\bar{\tau}_{xz}$	$\bar{\tau}_{yz}$
4	TSDT [13]	0.5868	1.1959	0.7541	0.4913	0.4913	0.4304
	SSDPT [15]	0.5865	1.1988	0.7534	0.4909	0.4906	0.4307
	HSDT [20]	0.5872	1.1425	0.7617	0.5070	0.4695	0.4173
	Present	0.5869	1.1485	0.7656	0.5191	0.5685	0.4263
	TSDT [13]	0.4666	2.8920	1.9106	1.2855	0.4963	0.4411
	SSDPT [15]	0.4665	2.8932	1.9103	1.2850	0.5114	0.4429
10	HSDT [20]	0.4663	2.8560	1.9040	1.2660	0.4700	0.4174
	Present	0.4660	2.8711	1.9141	1.2966	0.5686	0.4264
	TSDT [13]	0.4438	28.7341	19.1543	12.9885	0.5004	0.4448
	SSDPT [15]	0.4438	28.7342	19.1543	13.0125	0.5164	0.4472
	HSDT [20]	0.4435	28.5600	19.0400	12.6500	0.4696	0.4174
	Present	0.4433	28.7115	19.1410	12.9558	0.5686	0.4264

The convergence study has demonstrated the effectiveness of the FE used in this analysis. The results show that the mesh refinement leads to more accurate outcomes, with the 24×24 mesh providing optimal accuracy for the static analysis and the 20×20 mesh being the most suitable choice for the buckling analysis, balancing accuracy and computational efficiency.

The following section presents numerical examples to further validate the performance of the proposed method and explore its application to different cases.

5.2. Static analysis

5.2.1. Example 1

The effect of the side thickness ratio is evaluated using a SSSS square FG plate with an aspect ratio of $L_x/L_y = 1$, and the volume fraction exponent set to $p = 0$. Results are compared with those obtained from the different approaches, Reddy's TSDT [13], Zenkour's SSDPT [15], and Tati's HSDT [20] (Table 4).

The displacement results show a close agreement between the present study and the other models. This is expected because, in bending analysis, the displacement of the plate is primarily governed by its geometry, material properties, and

BCs. As the side-to-thickness ratio increases, the displacement decreases. This is expected because larger L_x/h ratios result in a stiffer plate, causing less deflection under the same applied load. The very small differences observed, especially for lower values of L_x/h , can be attributed to the different approximations used in the models, particularly concerning shear deformation. However, the overall displacement behavior is similar, confirming that all models capture the fundamental bending response of the FG plate accurately.

The normal stresses $\bar{\sigma}_x$ and $\bar{\sigma}_y$, generally increase as the side-to-thickness ratio decreases. At smaller L_x/h values, the plate is more flexible, leading to higher bending-induced normal stresses, which is characteristic of thinner or more flexible plates. As L_x/h increases, the plate becomes stiffer, reducing the magnitude of normal stresses. These results are also in good agreement between the present study and the referenced models, with slight variations. These stresses are important for understanding the plate's response to bending loads, and the fact that the present study predicts slightly higher normal stresses can be attributed to the more detailed modeling of material inhomogeneity and the plate's mechanical response to bending. This higher stress could indicate a more refined capture of the stress distribution through the thickness of the plate, which is important in FGPs where the material properties vary spatially. The shear stress results show that for smaller L_x/h ratios (thinner plates), they increase due to reduced stiffness and greater deformations in the thickness direction. This is particularly evident for $\bar{\tau}_{xy}$, $\bar{\tau}_{xz}$, and $\bar{\tau}_{yz}$ at $L_x/h = 4$, where shear stresses are higher compared to the reference models like Tati [20]. This suggests that the present model, which better accounts for shear deformation effects, provides a more accurate prediction of the behavior of FGPs, especially for thinner plates. This trend confirms the physical theory that thinner plates experience larger deformations, leading to higher shear stresses, and highlights the improvement of the present approach over traditional models.

5.2.2. Example 2

This example involves an SSSS FG plate subjected to UDL with a side-to-thickness ratio of 10. Figures 8–10 illustrate the variation of the in-plane stress $\bar{\sigma}_x$, $\bar{\tau}_{xy}$, and the transverse shear stress $\bar{\tau}_{xz}$, respectively, through the plate thickness z/h for different values of p , which governs the material distribution within the FG plate. The horizontal axis represents the relative position across the plate's thickness, ranging from the bottom surface to the top surface, while the vertical axis shows the corresponding stresses, where positive values indicate tension and negative values represent compression. For all cases, it is observed that the neutral plane, where the stress becomes zero, shifts further away from the mid-plane of the plate as the gradient parameter p increases. When $p = 0$, corresponding to fully ceramic homogeneous plates, the in-plane normal stress distribution through the thickness is almost linear, with the stress vanishing at the mid-plane, as highlighted by Singha et al. [8]. In this scenario, the transverse shear stress follows a perfectly parabolic

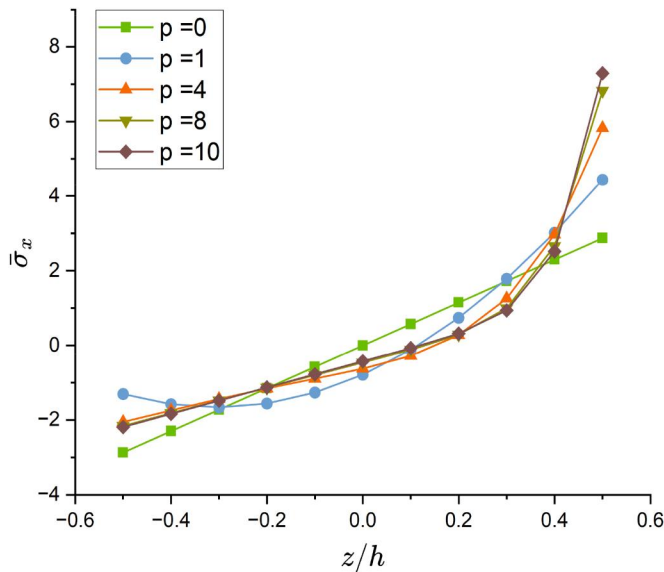


Figure 8. Change in The nondimensional in-plane stress of the FG square plate subjected to UDL for various values of p ($L_x/h = 10$).

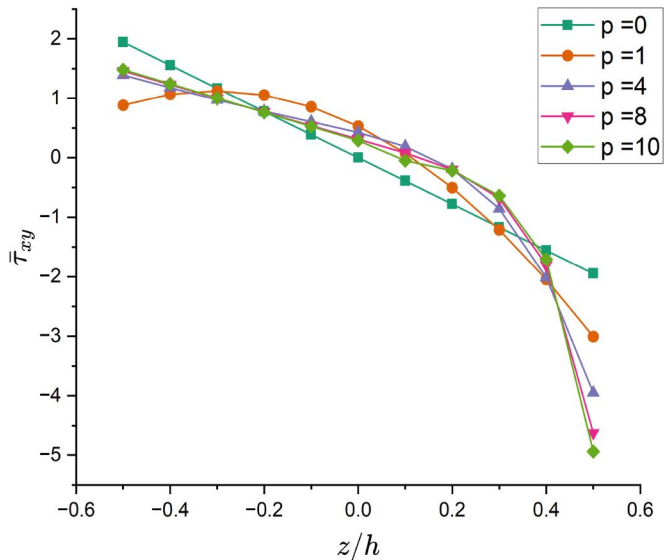


Figure 9. Change in the nondimensional in-plane shear stress of the FG square plate subjected to UDL for various values of p ($L_x/h = 10$).

distribution. As the material composition becomes more graded with higher values of p , the stress distribution undergoes significant changes, influencing how the plate carries the applied load and underscoring the importance of material gradation in the mechanical behavior of FGPs.

5.2.3. Example 3

To evaluate the effect of the power law index p on the FG plate behavior, the nondimensional central deflections and stresses for various values of p of an SSSS square FG plate are summarized in **Table 5**. Results are compared for various theories for different values of the volume fraction exponent p . It can be observed that the displacement remains almost constant across all methods, with slight variations. The in-plane normal stresses $\bar{\sigma}_x$ and $\bar{\sigma}_y$ increase with the value of p , indicating higher stresses as the material composition

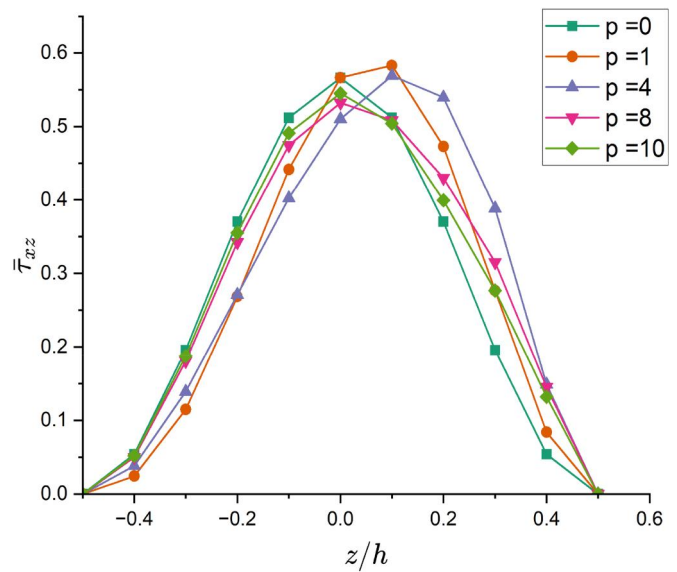


Figure 10. The nondimensional transverse shear stress variation of the FG square plate subjected to UDL for various values of p ($L_x/h = 10$).

Table 5. Variation of dimensionless stresses and displacements of FG square plate subjected to UDL for various volume fraction exponent values ($L/h = 10$).

p	Theory	\bar{w}	$\bar{\sigma}_x$	$\bar{\sigma}_y$	$\bar{\tau}_{xy}$	$\bar{\tau}_{xz}$	$\bar{\tau}_{yz}$
0	SSDPT [15]	0.4665	2.8932	1.9103	1.2850	0.5114	0.4429
	HSDT [20]	0.4663	2.8560	1.9040	1.2660	0.4696	0.4174
	Quasi-3D HSDT [18]	0.4635	2.9981	1.8925	1.2578	0.4782	0.4315
	SBFEM [5]	0.4662	2.8249	1.8870	1.2759	0.4966	0.4980
	Present	0.4660	2.8711	1.9141	1.2966	0.5686	0.4264
1	SSDPT [15]	0.9287	4.4745	2.1692	1.1143	0.5114	0.5446
	HSDT [20]	0.9282	4.4150	2.1640	1.0930	0.4696	0.5133
	Quasi-3D HSDT [18]	0.8977	4.6110	2.0822	1.0211	0.4782	0.5119
	SBFEM [5]	0.9212	4.4030	2.1572	1.1061	0.4882	0.5418
	Present	0.9277	4.4376	2.1752	1.1197	0.5685	0.5243
2	SSDPT [15]	1.1940	5.2296	2.0338	0.9907	0.4700	0.5734
	HSDT [20]	1.1948	5.1550	2.0320	0.9745	0.4368	0.5469
	Quasi-3D HSDT [18]	1.1376	5.3825	1.9257	0.8921	0.4524	0.5081
	SBFEM [5]	1.1956	5.2970	1.9784	0.9708	0.4479	0.5413
	Present	1.1959	5.1815	2.0426	0.9979	0.5456	0.5764
4	SSDPT [15]	1.3890	5.8915	1.7197	1.0298	0.4204	0.5346
	HSDT [20]	1.3916	5.7970	1.7240	1.0160	0.3926	0.5124
	Quasi-3D HSDT [18]	1.3259	6.0382	1.6062	0.9274	0.4358	0.4804
	SBFEM [5]	1.3779	5.9532	1.7204	1.0335	0.4187	0.5105
	Present	1.3974	5.8272	1.7325	1.0293	0.5132	0.5652
10	SSDPT [15]	1.5876	7.3689	1.2820	1.0694	0.4552	0.4227
	HSDT [20]	1.5934	7.2530	1.2880	1.0580	0.4298	0.4096
	Quasi-3D HSDT [18]	1.5453	7.5123	1.2016	0.9860	0.4332	0.4561
	SBFEM [5]	1.5604	7.2217	1.2203	1.1056	0.4487	0.4207
	Present	1.5988	7.2908	1.2943	1.0834	0.5489	0.4414

becomes more graded. The shear stresses also show similar trends, with values for the present method generally being slightly higher than those from other methods, especially for higher p . This indicates that as the material becomes more functionally graded, the distribution of normal and shear stresses is more uneven, which physically reflects the increased variation in material properties across the plate thickness. Specifically, the neutral plane, where stress is zero, shifts further away from the mid-plane as p increases, highlighting the significant role of material gradation in the overall stress distribution. This behavior underlines the influence of material composition on how the plate carries the applied load, with more graded materials leading to more pronounced variations in the stress distribution,

especially in the shear components. The results of the present element show accuracy and effectively capture the complex behavior of the FG plate, providing a reliable representation of the stress distribution across varying material gradations.

5.2.4. Example 4

To evaluate the BCs effect on the FG plate's behavior, Table 6 presents the maximum nondimensional deflections of square FG plate under distinct boundary constraints, which are indicated by the abbreviations, as shown in Table 1. The power-law index values differ for each situation.

As the parameter p increases, the central deflection increases for all BCs, with the simply supported (SSSS) plate exhibiting the highest deflection values, indicating greater flexibility. In contrast, the clamped plate (CCCC) shows the smallest deflections, reflecting its higher stiffness. The mixed BCs (SCSC, SFSC, SFSS, SSSC) yield intermediate results, with deflections between those of the fully simply supported and fully clamped plates. The trends highlight the influence of BCs on the plate's deflection response, where more restrictive BCs lead to lower central deflections, and less restrictive conditions allow for greater displacement.

Figures 11 and 12 illustrate the deflection distribution for a square FG plate with $p=0$, subjected to two BCs: SSSS and CCCC. These two cases were selected as they represent extreme scenarios in terms of edge stiffness. Figure 11 shows a higher maximum deflection for the SSSS case, which can be attributed to the flexibility of the edges, allowing more pronounced bending and making the plate more sensitive to

Table 6. The maximum nondimensional deflection of the FG plate as a function of p and the various BCs.

p	CCCC	SSSS	SCSC	SFSC	SFSS	SSSC
0	0.1639	0.4660	0.2405	0.5781	0.7809	0.3334
1	0.3208	0.9277	0.4726	1.1428	1.5513	0.6596
4	0.5065	1.3974	0.7379	1.7532	2.3479	1.0108
5	0.5300	1.4460	0.7702	1.8213	2.4314	1.0503
10	0.5941	1.5988	0.8605	2.0232	2.6902	1.1672

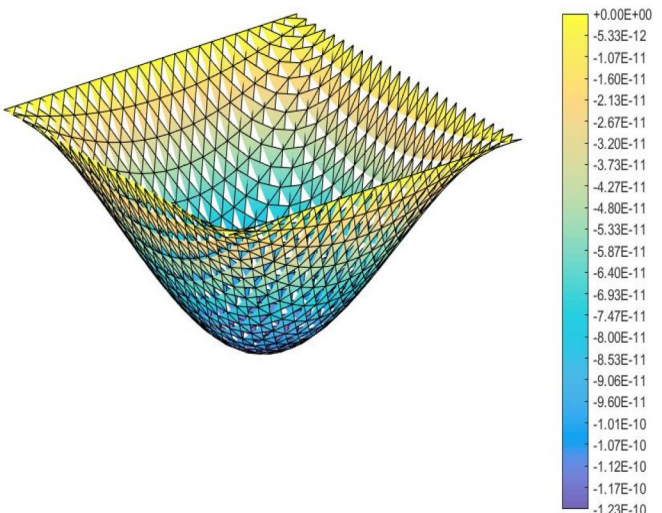


Figure 11. Deflection distribution of a square FG plate under SSSS BCs for $p=0$.

the graded material properties. Conversely, Figure 12 depicts a significantly reduced maximum deflection for the CCCC case, due to the increased edge rigidity that restricts displacements and enhances the dissipation of internal stresses. From a physical perspective, this highlights the interaction between the FG plate properties and the BCs: in the SSSS case, the gradual transition of material properties has a more pronounced influence on the mechanical response of the plate, whereas in the CCCC case, the rigidity imposed by the clamped edges dominates, limiting the effect of the material gradation.

5.3. Buckling analysis

The study of the buckling behavior in FGPs is crucial for understanding their behavior under complex loading conditions. FGPs, with properties that vary continuously across their thickness, exhibit distinct buckling behaviors compared to traditional homogeneous plates. This study focuses on analyzing and predicting the buckling response of FGPs based on factors such as power law index p , BCs, plate properties, and different in plane loading types (see Figure 13) aiming to optimize structural performance.

5.3.1. Example 5

This example demonstrates the effect of the power-law index p and the side-to-thickness ratio L_x/h of an FG SSSS square plate under uniaxial and biaxial loading with an aspect ratio of 1. The results, provided in Tables 7 and 8, highlight the effectiveness of the element, showing convergence with well-established and highly cited references.

For uniaxial loading, as L_x/h increases, the plate becomes thinner, resulting in a lower stiffness and subsequently lower critical buckling loads, which is consistent with the expected behavior of plates under compressive loading. Similarly, as the power-law index p increases, the material distribution shifts, with more material transitioning to a weaker phase, leading to a further reduction in stiffness and critical buckling loads. The

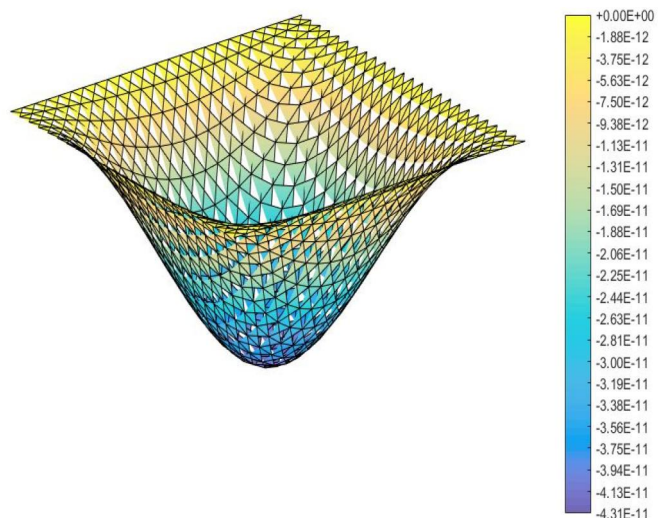


Figure 12. Deflection distribution of a square FG plate under CCCC BCs for $p=0$.

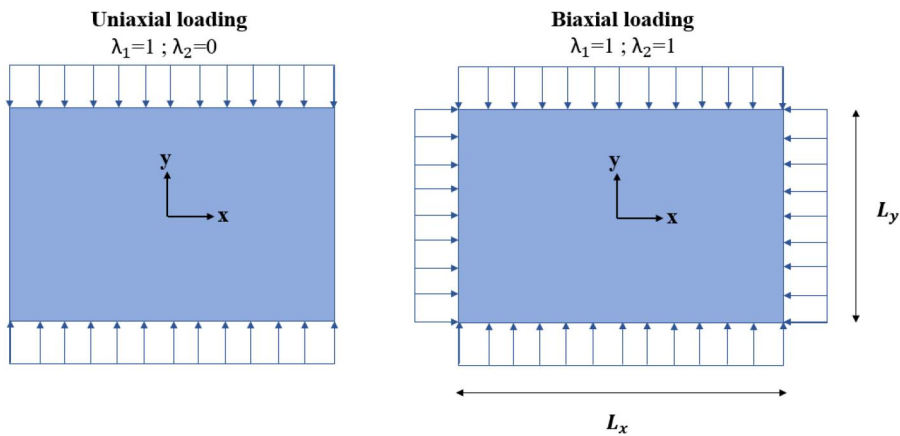


Figure 13. Uniaxial and biaxial loading conditions.

Table 7. Dimensionless critical buckling load \bar{N}_{cr} of an FGM plate under uniaxial loading ($\lambda_1=1$, $\lambda_2=0$) ($L_x/L_x=1$).

L_x/h	Source	$p=0$	$p=1$	$p=2$	$p=5$	$p=10$	$p=20$
5	HSDT [21]	16.0582	8.2448	6.3250	5.0010	4.4178	3.9509
	HSDT [25]	16.0211	8.2245	6.3432	5.0531	4.4807	4.0070
	HSDT [26]	16.00	8.146	6.2300	4.9700	4.4400	3.9800
	RHSDT [62]	16.0210	8.2244	6.3431	5.0530	4.4806	4.0069
	Present	15.9967	8.2119	6.2661	4.8879	4.3431	3.9222
10	HSDT [21]	18.6385	9.3696	/	6.0323	5.4435	4.8265
	HSDT [25]	18.5785	9.3391	/	6.0353	5.4528	4.8346
	HSDT [26]	18.5400	9.2990	7.2100	5.990	5.4200	4.8200
	RHSDT [62]	18.5785	9.3391	7.2630	6.0353	5.4528	4.8346
	Present	18.5511	9.3250	7.2302	5.9696	5.3962	4.7989
50	HSDT [21]	19.6486	9.7971	7.6433	6.4584	5.8803	5.1948
	HSDT [25]	19.5814	9.7636	7.6177	6.4373	5.8614	5.1782
	HSDT [26]	19.5400	9.7430	7.6010	6.4200	5.8400	5.1600
	RHSDT [62]	19.5814	9.7636	7.6176	6.4372	5.8613	5.1781
	Present	19.5496	9.7477	7.6045	6.4242	5.8495	5.1684
100	HSDT [21]	19.6812	9.8107	7.6551	6.4724	5.8949	5.2071
	HSDT [25]	19.6145	9.7775	7.6293	6.4507	5.8752	5.1897
	HSDT [26]	19.5700	9.7500	7.6100	6.4300	5.8600	5.1700
	RHSDT [62]	19.6145	9.7775	7.6293	6.4507	5.87515	5.1896
	Present	19.5827	9.7615	7.9711	6.4396	5.8652	5.1810

Table 8. Dimensionless critical buckling load \bar{N}_{cr} of an FGM plate under biaxial loading ($\lambda_1=1$, $\lambda_2=1$) ($L_x/L_x=1$).

L_x/h	Source	$p=0$	$p=1$	$p=2$	$p=5$	$p=10$	$p=20$
5	HSDT [21]	8.0291	4.1224	3.1625	2.5005	2.2089	1.9754
	HSDT [25]	8.0110	4.1120	3.1720	2.5270	2.2400	2.0040
	HSDT [26]	8.0010	4.0730	3.1200	2.4870	2.2210	1.9940
	RHSDT [62]	8.0105	4.1122	3.1715	2.5265	2.2403	2.0034
	Present	7.9984	4.1060	3.1331	2.4440	2.1715	1.9611
10	HSDT [21]	9.3193	4.6848	3.6379	3.0161	2.7217	2.4132
	HSDT [25]	9.2890	4.6700	3.6320	3.0180	2.7346	2.4170
	HSDT [26]	9.2730	4.6500	3.6080	2.9980	2.7150	2.4100
	RHSDT [62]	9.2892	4.6695	3.6315	3.0176	2.7264	2.4173
	Present	9.2756	4.6625	3.6151	2.9848	2.6981	2.3994
50	HSDT [21]	9.8243	4.8986	3.8217	3.2292	2.9401	2.5974
	HSDT [25]	9.7910	4.8820	3.8090	3.2190	2.9310	2.5890
	HSDT [26]	9.7720	4.8720	3.8010	3.2120	2.9250	2.5840
	RHSDT [62]	9.7907	4.8818	3.8088	3.2186	2.9306	2.5890
	Present	9.7748	4.8739	3.8022	3.2121	2.9248	2.5842
100	HSDT [21]	9.8406	4.9053	3.8275	3.2362	2.9474	2.6035
	HSDT [25]	9.8070	4.8890	3.8150	3.2250	2.9380	2.5950
	HSDT [26]	9.7880	4.8790	3.8070	3.2190	2.9320	2.5900
	RHSDT [62]	9.8072	4.8887	3.8146	3.2253	2.9375	2.5948
	Present	9.7913	4.8808	3.9856	3.2198	2.9326	2.5905

present FEM demonstrates excellent agreement with reference results from the literature, with minor deviations, validating its accuracy and reliability. This example clearly demonstrates the effectiveness of the present element in accurately capturing the

combined influences of geometry and material gradation on the buckling behavior of FGPs.

The results for a square FG plate under biaxial loading are shown in Table 8. As L_x/h increases, the plate becomes thinner, leading to higher nondimensional buckling loads, which stabilize for larger thickness ratios. Similarly, as the power-law index p increases, the critical buckling load decreases due to the reduced stiffness caused by the redistribution of material toward a weaker phase. The present FEM closely matches the well-established results of Zenkour and Aljadani [61], with minor deviations validating its accuracy and efficiency.

Physically, the increase in L_x/h reduces the plate's stiffness, making it more prone to deformations, which is why thinner plates require higher normalized loads to reach buckling. The power-law index p reflects the material gradation; higher values lead to a softer material distribution, lowering the critical buckling resistance. These behaviors underline the influence of both geometry and material properties on the stability of FG plate under biaxial compressive loads.

5.3.2. Example 6

This example illustrates the influence of the power-law index and the side-to-thickness ratio on the nondimensional critical buckling load of an SSSS FG plate under uniaxial loading, as presented in Table 9, and biaxial loading, as shown in Table 10, for an aspect ratio $L_x/L_y = 2$. The obtained results demonstrate a high level of agreement with well-established and extensively cited references, including those of Tati's HSDT [21], Thai and Choi's HSDT [25], Reddy's analytical formulation using the HSDT [26], and Zenkour's refined HSDT [61], thereby validating the accuracy and robustness of the present analysis.

Table 9 presents the nondimensional critical buckling loads under uniaxial loading. As the side-to-thickness ratio increases, the plate becomes stiffer, leading to higher critical buckling loads. The results show a consistent trend: as the thickness of the plate increases, it exhibits improved resistance to buckling, especially under varying power-law indices. These findings align with the results from established references, validating the accuracy and efficiency of the current element. The comparison with well-established literature highlights the reliability of the present approach in capturing the buckling behavior of the FG plate.

Table 9. Dimensionless critical buckling load \bar{N}_{cr} of an FGM plate under uniaxial loading ($\lambda_1=1$, $\lambda_2=0$) ($L_x/L_y=2$).

L_x/h	Source	$p=0$	$p=1$	$p=2$	$p=5$	$p=10$	$p=20$
5	HSDT [21]	37.4695	20.6243	15.1896	10.2670	8.4837	7.7890
	HSDT [25]	37.7400	20.7400	15.5800	10.9500	9.1500	8.3900
	HSDT [26]	37.6700	20.2900	14.9900	10.6500	9.0400	8.3170
	RHSDT [62]	37.7403	20.7490	15.5819	10.9554	9.1505	8.3987
	Present	37.3897	20.5730	14.8826	9.6676	8.1538	7.7132
10	HSDT [21]	64.3349	33.0332	25.2409	20.0340	17.6971	15.8270
	HSDT [25]	64.0800	32.8900	25.3700	20.2100	17.9200	16.0200
	HSDT [26]	63.7800	32.8979	24.8600	19.8400	17.7200	15.9000
	RHSDT [62]	64.0842	32.4600	25.3726	20.2122	17.9227	16.0279
	Present	63.6460	32.6602	24.9287	19.4641	17.2989	15.6188
50	HSDT [21]	78.2169	39.0419	30.4404	25.6568	23.3324	20.6227
	HSDT [25]	77.8000	38.8300	30.2800	25.5300	23.2270	20.5300
	HSDT [26]	77.2000	38.5100	30.0200	25.3200	23.0400	20.3600
	RHSDT [62]	77.8003	38.8337	30.2857	25.5363	23.2278	20.5301
	Present	77.0311	38.4494	29.9709	25.2452	22.9650	20.3081
100	HSDT [21]	78.7471	39.2647	30.6328	25.8836	23.5667	20.8197
	HSDT [25]	78.3200	39.0500	30.4700	25.7400	23.4500	20.7100
	HSDT [26]	77.7100	38.7400	30.2200	25.5400	23.2600	20.5500
	RHSDT [62]	78.3256	39.0545	30.4707	25.7491	23.4455	20.7126
	Present	77.5402	38.6624	30.1619	25.4809	23.2018	20.4944

Table 10. Dimensionless critical buckling load \bar{N}_{cr} of an FG plate under biaxial loading ($\lambda_1 = \lambda_2 = 1$) ($L_x/L_y = 2$).

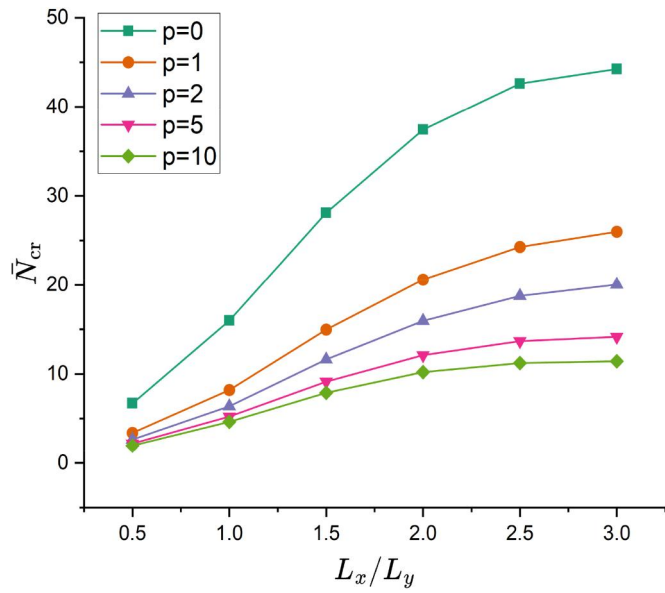
L_x/h	Source	$p=0$	$p=1$	$p=2$	$p=5$	$p=10$	$p=20$
5	HSDT [21]	15.7363	8.3198	6.2748	4.6628	4.0144	3.6271
	HSDT [25]	15.7240	8.3090	6.3350	4.7750	4.1380	3.7390
	HSDT [26]	15.6980	8.1720	6.1560	4.6610	4.0880	3.7120
	RHSDT [62]	15.7234	8.3091	6.3353	4.7753	4.1382	3.7392
	Present	15.7429	8.3211	6.2090	4.5024	3.9201	3.6049
10	HSDT [21]	21.5960	10.9800	8.4710	6.8448	6.1048	5.4386
	HSDT [25]	21.5050	10.9320	8.4640	6.8750	6.1480	5.4770
	HSDT [26]	21.4290	10.8300	8.3450	6.7820	6.0950	5.4440
	RHSDT [62]	21.5049	10.9323	8.4643	6.8749	6.1481	5.4768
	Present	21.5590	10.9588	8.4251	6.7460	6.0405	5.4176
50	HSDT [21]	24.5172	12.2313	9.5394	8.0503	7.3254	6.4731
	HSDT [25]	24.3940	12.1700	9.4930	8.0130	7.2930	6.4440
	HSDT [26]	24.2760	12.1080	9.4420	7.9700	7.2550	6.4120
	RHSDT [62]	24.3944	12.1699	9.4931	8.0132	7.2925	6.4440
	Present	24.4379	12.1918	9.5070	8.0196	7.2986	6.4515
100	HSDT [21]	24.6209	12.2748	9.5770	8.0948	7.3714	6.5117
	HSDT [25]	24.4970	12.2130	9.5290	8.0550	7.3350	6.4800
	HSDT [26]	24.3780	12.5820	9.4820	8.0150	7.5150	6.4480
	RHSDT [62]	24.4974	12.2132	9.5293	8.0549	7.3353	6.4798
	Present	24.5404	12.2345	9.5455	8.0670	7.3464	6.4902

For the biaxial loading, the results are presented in Table 10. As the value of L_x/h increases, the plate becomes thinner, leading to a decrease in critical buckling loads across all values of p , which is consistent with the general behavior of thin plates under biaxial loading. Specifically, for smaller values of p , the nondimensional critical buckling load is higher, but it decreases as p increases, indicating a softer response of the material. The results obtained in this study are in excellent agreement with established references, confirming the validity and accuracy of the present analysis in predicting the buckling behavior of the FGPs.

5.3.3. Example 7

To evaluate the effect of the aspect ratio, Figures 13 and 14 present the variation in the nondimensional critical buckling load for a SSSS FG plate under uniaxial and biaxial loading, respectively, with a side to thickness ratio $L_x/h = 5$.

Figure 14 shows the variation of the nondimensional critical buckling load for an FG plate under uniaxial

**Figure 14.** Effect of the aspect ratio on the nondimensional critical buckling load N_{cr} of a SSSS FG plate under uniaxial loading for various values of p .

compression for different power-law index. As L_x/L_y increases, the critical buckling load increases for all values of p . The curve corresponding to $p=0$ (uniform material distribution) shows the steepest increase in \bar{N}_{cr} as the aspect ratio increases. Conversely, as p increases, corresponding to a more rigid material distribution with stiffer material near the top surface, the rate of increase in critical buckling load is more gradual.

This behavior suggests that for higher values of p , the plate becomes stiffer, and thus, a larger aspect ratio is required to trigger buckling. The increase in \bar{N}_{cr} with L_x/L_y indicates that as the plate's dimensions become more elongated, the structural resistance to buckling increases, especially for plates with higher values of p , which have a higher concentration of stiffer material near the surface.

Figure 15 represents the same square FG plate but under biaxial loading, with a similar aspect ratio. The behavior of the curves is somewhat similar to the first graph, with the critical buckling load increasing as the aspect ratio grows. However, the values of the critical buckling load are consistently lower in comparison to the uniaxial loading case for all values of p . This can be attributed to the biaxial loading condition, which induces additional internal forces and makes the plate more susceptible to buckling at lower aspect ratios compared to the uniaxial case.

For all values of p , the trend shows a steady increase in \bar{N}_{cr} with increasing aspect ratio, but the increase is more moderate compared to the uniaxial case. Additionally, the plates with higher values of p show a more gradual slope, similar to the uniaxial case, indicating that as the material becomes stiffer, the critical buckling load increases more gradually with the aspect ratio. The biaxial loading condition results in lower critical loads for the same aspect ratio compared to the uniaxial loading, further illustrating the role of the loading type in influencing buckling behavior.

5.3.4. Example 8

To evaluate the effect of the BCs on the nondimensional critical buckling load, a study has been conducted. Figure 16 shows the nondimensional critical buckling loads for a square FG plate under uniaxial loading, with a side-to-thickness ratio of 10. The graph plots the critical buckling loads against the power-law index p for the different BCs denoted by their

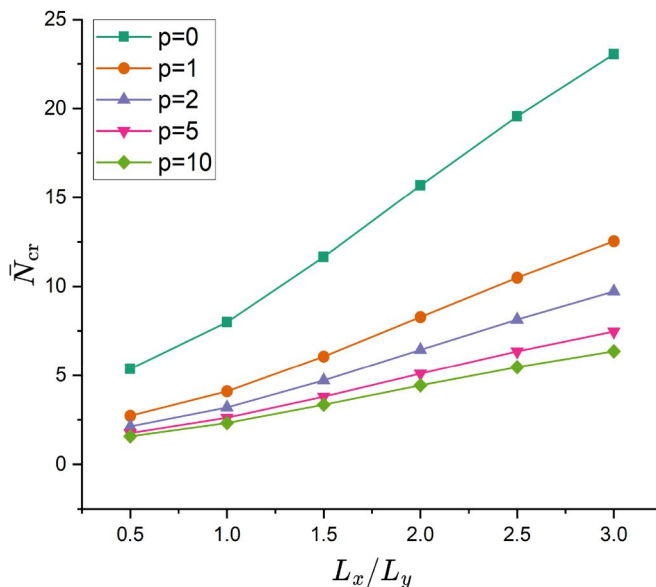


Figure 15. Effect of the aspect ratio on the nondimensional critical buckling load \bar{N}_{cr} of a SSSS FG plate under biaxial loading for various values of p .

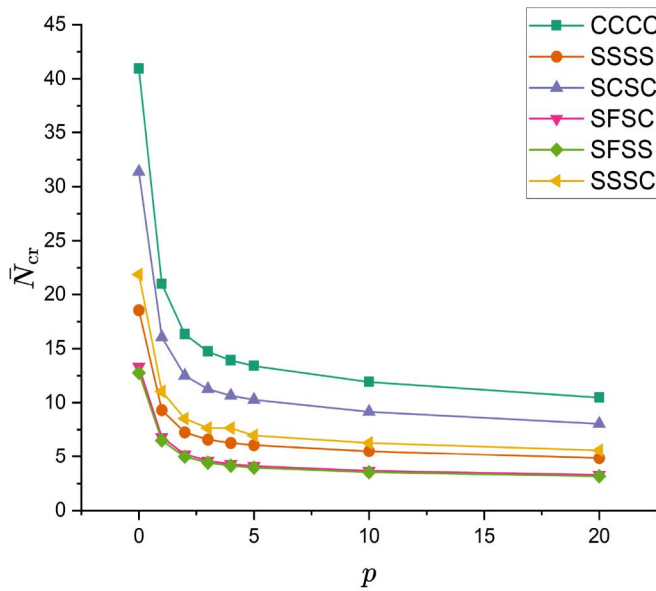


Figure 16. Effect of the BCs on the nondimensional critical buckling load \bar{N}_{cr} for various values of p .

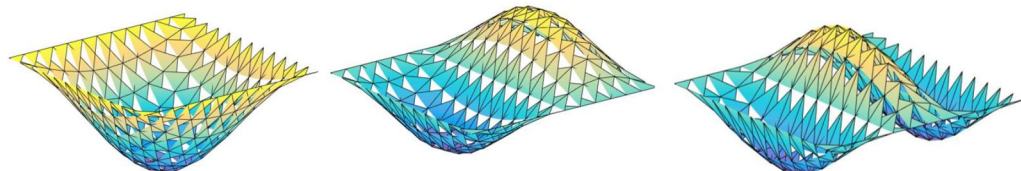


Figure 17. First three buckling modes of SSSS FG square plate under uniaxial loading.

abbreviation for simplicity (see Table 1). As the power-law index increases, the critical buckling load decreases for all BCs, indicating that higher values of p , which correspond to more rigid material distributions, result in reduced buckling resistance. This behavior can be attributed to the change in material properties along the plate thickness, where increasing p leads to a higher concentration of stiffer material near the top surface, making the plate more susceptible to buckling. The results for the different BCs follow a similar trend, with the CCCC BCs exhibiting the highest critical buckling loads, as expected for a fully clamped plate, and the SFSS and SFSC BCs showing the lowest values. These results highlight the strong influence of BCs and the power-law index on the buckling behavior of FGPs under uniaxial loading.

5.3.5. Example 9

To illustrate the effect of the type of loading, uniaxial versus biaxial, Figures 17 and 18 show the first three buckling modes of SSSS square FG plate. Figure 17 presents the modes under uniaxial loading, while Figure 18 depicts the modes under biaxial loading. These figures highlight the influence of the loading type on the buckling behavior and deformation patterns of the plate.

Under uniaxial loading, the first buckling mode exhibits a symmetric bowl-like deformation, representing the primary instability pattern at the critical load. As the load increases, the second mode emerges with additional waves perpendicular to the loading direction, indicating a higher complexity in the deformation behavior. The third mode further amplifies this complexity, displaying multiple waves and larger amplitudes in certain regions, which reflect the influence of the plate's geometry and the graded material properties.

Under biaxial loading, the first buckling mode takes on a dome-like or ridge-shaped deformation, showing a more uniform distribution of instability along both axes. In the second mode, additional waves appear in both directions, demonstrating a coupling effect between the biaxial loads and the anisotropic nature of the FGM. The third mode reaches maximum complexity, with more frequent and pronounced deformations in both directions, highlighting the increased instability caused by the combined loading conditions.

A comparison of the two loading cases reveals that uniaxial loading results in more directional and asymmetric deformation patterns, with waves concentrated perpendicular to the loading direction. In contrast, biaxial loading produces more uniform and symmetric deformation patterns, with waves distributed along both axes. This demonstrates that biaxial loading induces a more complex yet balanced buckling response compared to the localized effects seen under uniaxial loading.

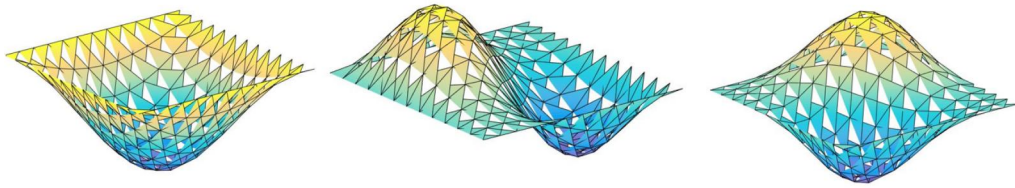


Figure 18. First three buckling modes of SSSS FG square plate under biaxial loading.

6. Real-world application of the developed element

The newly developed strain-based FEM using a sinusoidal shear deformation theory offers numerous advantages across various engineering fields. In aerospace engineering, it enables the design of lightweight, high-performance components like fuselage panels, wings, and thermal protection systems, with improved accuracy in stress and deflection predictions, ensuring structural integrity under extreme flight conditions. In civil engineering, this method optimizes composite bridge decks, large-span roofs, and high-rise buildings by ensuring better load distribution and material efficiency while maintaining stability, especially under seismic and wind loads. In marine engineering, the approach provides accurate modeling of ship hulls, submarines, and offshore platforms, capturing the effects of dynamic oceanic pressures and high-stress conditions, enhancing safety and durability. In biomedical engineering, it improves the design of prosthetics, implants, and FG bone plates, offering better stress distribution, improved mechanical performance, and compatibility with biological tissues. In automotive engineering, it enhances the design of crash-resistant panels and chassis, providing insights into deformation and stress distribution during impact, improving safety, and performance.

The key advantages of the developed element include its ability to accurately model shear deformation without the need for shear correction factors, providing a more realistic representation of material behavior. Additionally, the sinusoidal shear deformation theory allows for a more precise prediction of deflections and stress distributions, particularly in thick plates and structures with steep material gradients. This method is computationally efficient, offering an improved balance between accuracy and computational cost, making it ideal for complex geometries and BCs. Furthermore, it eliminates the limitations of traditional shear deformation theories, providing a higher level of precision and reliability in both static and dynamic analyses, thus, enabling optimized designs and improved performance across diverse applications.

7. Conclusion

The developed FE model HSBFGQP resulting from the combination of the membrane element which contains two DOFs and the bending element with his three DOFs, is used to evaluate the static and the buckling analysis of the FG plates integrating the strain-based approach with the newly developed HSDT. The model assumes a sinusoidal distribution of lateral shear stress across the plate thickness, with the shear stress being zero at the free boundaries. Following a power-law function, the properties of FGPs change gradually with the volume fraction of their components along the thickness direction. To eliminate

stretching-bending coupling, the neutral surface concept is utilized. Additionally, the shear deformation energy, derived from both the three-dimensional elasticity theory and the Reissner-Mindlin theory, is compared to develop the new sinusoidal function, which plays a key role in reducing the number of unknowns from six to five. The concept of potential energy is applied to express the stiffness and geometric matrices. The effectiveness of the novel FE model in analyzing the static and buckling behaviors of FGPs has been validated through comparison with published test results. The study explores the influence of various factors on the static and buckling responses of FGPs, such as side-to-thickness ratio, power-law index, plate thickness, aspect ratio, BCs and the type of loading. Some of the observed effects include:

- Static Behavior:

Displacement decreases as the side-to-thickness ratio (L_x/h) increases, reflecting greater plate stiffness. Thinner plates (lower L_x/h), conversely, experience higher normal and shear stresses due to their reduced stiffness. The model captures these effects accurately, particularly through its detailed representation of material inhomogeneity. Additionally, the stress distribution is significantly influenced by the power-law index, with higher p values shifting the neutral plane and increasing stresses. Furthermore, BCs play a critical role, as more restrictive BCs reduce deflections, while higher p values lead to increased central deflection across all BCs.

- Buckling Behavior:

In terms of buckling, critical buckling loads decrease with higher L_x/h and power-law index p , primarily due to reduced stiffness and the redistribution of material properties. Clamped plates exhibit the highest buckling resistance, whereas simply supported plates show lower resistance. Under biaxial loading, critical buckling loads stabilize at larger thickness ratios but decrease with higher p values. Notably, uniaxial loading results in asymmetric buckling patterns, while biaxial loading produces a more uniform and symmetric response, highlighting the significant influence of loading conditions on the instability behavior of functionally graded plates.

The presented FE model is a powerful tool for simulating FGPs and will be expanded in the future to include free vibration analysis of FGPs and FG shell structures. This extension will improve the understanding of stability under various loading conditions and material distribution effects. It will also aid in the design of lightweight, high-performance structures in fields such as aerospace, automotive, and civil engineering by addressing the complex interactions between geometry and material properties.

Disclosure statement

No potential conflict of interest was reported by the authors.

Funding

This research received no specific grant from funding agencies in any sector.

ORCID

Madjda Chenafi  <http://orcid.org/0009-0003-6849-6735>
 Messaoud Bourezane  <http://orcid.org/0009-0002-3065-7620>
 Taqiyeddine Assas  <http://orcid.org/0009-0001-4288-2908>
 Abdelouahab Tati  <http://orcid.org/0000-0001-5408-3970>

References

- [1] D.T. Thuy, L.N. Ngoc, D.N. Tien, and H.V. Thanh, An analytical solution for the dynamics of a functionally graded plate resting on viscoelastic foundation, *Eng. Technol. Appl. Sci. Res.*, vol. 13, no. 1, pp. 9926–9931, 2023. DOI: [10.48084/etatr.5420](https://doi.org/10.48084/etatr.5420).
- [2] J. Singh, A. Kumar, M. Szafraniec, D. Barnat-Hunek, and B. Sadowska-Buraczewska, Static analysis of skew functionally graded plate using novel shear deformation theory, *Materials*, vol. 15, no. 13, pp. 4633, 2022. DOI: [10.3390/ma15134633](https://doi.org/10.3390/ma15134633).
- [3] A.K. Sharma, P. Sharma, P.S. Chauhan, and S.S. Bhadoria, Study on harmonic analysis of functionally graded plates using FEM, *Int. J. Appl. Mech. Eng.*, vol. 23, no. 4, pp. 941–961, 2018. DOI: [10.2478/ijame-2018-0053](https://doi.org/10.2478/ijame-2018-0053).
- [4] G.T. Mohammed Nabi Anwarbasha, A. Chakrabarti, A. Bahrami, V. Venkatesan, A.S.V. Vikram, J. Subramanian, and V. Mahesh, Efficient finite element approach to four-variable power-law functionally graded plates, *Buildings*, vol. 13, no. 10, pp. 2577, 2023. DOI: [10.3390/buildings13102577](https://doi.org/10.3390/buildings13102577).
- [5] W. Ye, J. Liu, J. Zhang, F. Yang, G. Lin Method', and Vol, J., A new semi-analytical solution of bending, buckling and free vibration of functionally graded plates using scaled boundary finite element, *Thin-Walled Struct.*, vol. 163, pp. 107776, 2021. DOI: [10.1016/j.tws.2021.107776](https://doi.org/10.1016/j.tws.2021.107776).
- [6] R.D. Mindlin, Influence of rotatory inertia and shear on flexural motions of isotropic, elastic plates, *J. Appl. Mech.*, vol. 18, no. 1, pp. 31–38, 1951. DOI: [10.1115/1.4010217](https://doi.org/10.1115/1.4010217).
- [7] J.N. Reddy, Mechanics of Laminated Composite Plates and Shells: Theory and Analysis, 2nd Ed., CRC Press, Boca Raton, FL, USA, 2003.
- [8] M.K. Singha, T. Prakash, and M. Ganapathi, Finite element analysis of functionally graded plates under transverse load, *Finite Elem. Anal. Des.*, vol. 47, no. 4, pp. 453–460, 2011. DOI: [10.1016/j.finel.2010.12.001](https://doi.org/10.1016/j.finel.2010.12.001).
- [9] S. Natarajan, A.J.M. Ferreira, S. Bordas, E. Carrera, M. Cinefra, and A.M. Zenkour, Analysis of functionally graded material plates using triangular elements with cell-based smoothed discrete shear gap method, *Math. Probl. Eng.*, vol. 2014, no. 1, p. 247932, 2014. DOI: [10.1155/2014/247932](https://doi.org/10.1155/2014/247932).
- [10] H. Nguyen-Xuan, L.V. Tran, T. Nguyen-Thoi, and H.C. Vu-Do, Analysis of functionally graded plates using an edge-based smoothed finite element method, *Compos. Struct.*, vol. 93, no. 11, pp. 3019–3039, 2011. DOI: [10.1016/j.compstruct.2011.04.028](https://doi.org/10.1016/j.compstruct.2011.04.028).
- [11] H. Nguyen-Xuan, L.V. Tran, C.H. Thai, and T. Nguyen-Thoi, Analysis of functionally graded plates by an efficient finite element method with node-based strain smoothing, *Thin-Walled Struct.*, vol. 54, pp. 1–18, 2012. DOI: [10.1016/j.tws.2012.01.013](https://doi.org/10.1016/j.tws.2012.01.013).
- [12] B.A. Djalil, B. Hichem, B.A. Anis, and B.K. Halim, A new higher order shear and normal deformation theory for bending analysis of advanced composite plates, Third International Conference on Energy Materials Applied Energetics and Pollution (ICEMAEP'16), Constantin, Algeria, 2016.
- [13] J. Reddy, Analysis of functionally graded plates, *Int. J. Numer. Methods Eng.*, vol. 47, no. 1–3, pp. 663–684, 2000. DOI: [10.1002/\(SICI\)1097-0207\(20000110/30\)47:1/33.0.CO;2-8](https://doi.org/10.1002/(SICI)1097-0207(20000110/30)47:1/33.0.CO;2-8).
- [14] H. Matsunaga, Free vibration and stability of functionally graded plates according to a 2-D higher-order deformation theory, *Compos. Struct.*, vol. 82, no. 4, pp. 499–512, 2008. DOI: [10.1016/j.compstruct.2007.01.030](https://doi.org/10.1016/j.compstruct.2007.01.030).
- [15] A.M. Zenkour, Generalized shear deformation theory for bending analysis of functionally graded plates, *Appl. Math. Model.*, vol. 30, no. 1, pp. 67–84, 2006. DOI: [10.1016/j.apm.2005.03.009](https://doi.org/10.1016/j.apm.2005.03.009).
- [16] S. Hosseini-Hashemi, M. Fadaee, and S.R. Atashipour, Study on the free vibration of thick functionally graded rectangular plates according to a new exact closed-form procedure, *Compos. Struct.*, vol. 93, no. 2, pp. 722–735, 2011. DOI: [10.1016/j.compstruct.2010.08.007](https://doi.org/10.1016/j.compstruct.2010.08.007).
- [17] I. Mechab, B. Mechab, and S. Benissa, Static and dynamic analysis of functionally graded plates using four-variable refined plate theory by the new function, *Compos. B Eng.*, vol. 45, no. 1, pp. 748–757, 2013. DOI: [10.1016/j.compositesb.2012.07.015](https://doi.org/10.1016/j.compositesb.2012.07.015).
- [18] S.S. Akavci and A.H. Tanrikulu, Static and free vibration analysis of functionally graded plates based on a new quasi-3D and 2D shear deformation theories, *Compos. B Eng.*, vol. 83, pp. 203–215, 2015. DOI: [10.1016/j.compositesb.2015.08.043](https://doi.org/10.1016/j.compositesb.2015.08.043).
- [19] M. Talha and B.N. Singh, Static response and free vibration analysis of FGM plates using higher order shear deformation theory, *Appl. Math. Model.*, vol. 34, no. 12, pp. 3991–4011, 2010. DOI: [10.1016/j.apm.2010.03.034](https://doi.org/10.1016/j.apm.2010.03.034).
- [20] A. Tati, A five unknowns high order shear deformation finite element model for functionally graded plates bending behavior analysis, *J. Braz. Soc. Mech. Sci. Eng.*, vol. 43, no. 1, pp. 45, 2021. DOI: [10.1007/s40430-020-02736-1](https://doi.org/10.1007/s40430-020-02736-1).
- [21] A. Tati, Finite element analysis of thermal and mechanical buckling behavior of functionally graded plates, *Arch. Appl. Mech.*, vol. 91, no. 11, pp. 4571–4587, 2021. DOI: [10.1007/s00419-021-02025-w](https://doi.org/10.1007/s00419-021-02025-w).
- [22] A. Sadgui and A. Tati, A novel trigonometric shear deformation theory for the buckling and free vibration analysis of functionally graded plates, *Mech. Adv. Mater. Struct.*, vol. 29, no. 27, pp. 6648–6663, 2022. DOI: [10.1080/15376494.2021.1983679](https://doi.org/10.1080/15376494.2021.1983679).
- [23] A. Tati, A. Belounar, and A. Sadgui, Bending and free vibration analysis of FG circular plates using a five unknown high order shear deformation theory, *Mech. Based Des. Struct. Mach.*, vol. 52, no. 10, pp. 8116–8140, 2024. DOI: [10.1080/15397734.2024.2315173](https://doi.org/10.1080/15397734.2024.2315173).
- [24] A.M. Zenkour and M.H. Aljadani, Mechanical buckling of functionally graded plates using a refined higher-order shear and normal deformation plate theory, *Adv. Aircr. Spacecr. Sci.*, vol. 5, no. 6, pp. 615–632, 2018. DOI: [10.12989/aas.2018.5.6.615](https://doi.org/10.12989/aas.2018.5.6.615).
- [25] H.-T. Thai and D.-H. Choi, An efficient and simple refined theory for buckling analysis of functionally graded plates, *Appl. Math. Model.*, vol. 36, no. 3, pp. 1008–1022, 2012. DOI: [10.1016/j.apm.2011.07.062](https://doi.org/10.1016/j.apm.2011.07.062).
- [26] B.S. Reddy, J.S. Kumar, C.E. Reddy, and K.V.K. Reddy, Buckling analysis of functionally graded material plates using higher order shear deformation theory, *J. Compos.*, vol. 2013, pp. e808764–12, 2013. DOI: [10.1155/2013/808764](https://doi.org/10.1155/2013/808764).
- [27] M. Afzali, M. Farrokh, and E. Carrera, Nonlinear thermal post-buckling analysis of rectangular FG plates using CUF, *Compos. Struct.*, vol. 321, pp. 117282, 2023. DOI: [10.1016/j.compstruct.2023.117282](https://doi.org/10.1016/j.compstruct.2023.117282).
- [28] H. Chaabani, S. Mesmoudi, L. Boutahar, and K.E. Bikri, A high-order finite element continuation for buckling analysis of porous FGM plates, *Eng. Struct.*, vol. 279, pp. 115597, 2023. DOI: [10.1016/j.engstruct.2023.115597](https://doi.org/10.1016/j.engstruct.2023.115597).
- [29] M. Levy, Memoire sur la theorie des plaques elastiques planes, *Journal de mathématiques pures et appliquées*, vol. 3, pp. 219–306, 1877.
- [30] M. Stein, Vibration of beams and plate strips with three-dimensional flexibility, *J. Appl. Mech.*, vol. 56, no. 1, pp. 228–231, 1989. DOI: [10.1115/1.3176054](https://doi.org/10.1115/1.3176054).
- [31] A. Alnujaie, A.S. Sayyad, L. Hadji, and A. Tounsi, Buckling and free vibration analysis of multi-directional functionally graded

- sandwich plates, Struct. Eng. Mech., vol. 84, no. 6, 2022. DOI: [10.12989/sem.2022.84.6.813](https://doi.org/10.12989/sem.2022.84.6.813).
- [32] A.M.A. Neves, A.J.M. Ferreira, E. Carrera, M. Cinefra, R.M.N. Jorge, C.M. Mota Soares, and A.L. Araújo, Influence of zig-zag and warping effects on buckling of functionally graded sandwich plates according to sinusoidal shear deformation theories, Mech. Adv. Mater. Struct., vol. 24, no. 5, pp. 360–376, 2017. DOI: [10.1080/15376494.2016.1191095](https://doi.org/10.1080/15376494.2016.1191095).
- [33] A. Farzam and B. Hassani, A new efficient shear deformation theory for FG plates with in-plane and through-thickness stiffness variations using isogeometric approach, Mech. Adv. Mater. Struct., vol. 26, no. 6, pp. 512–525, 2019. DOI: [10.1080/15376494.2017.1400623](https://doi.org/10.1080/15376494.2017.1400623).
- [34] A.M. Zenkour, Exact relationships between classical and sinusoidal theories for FGM plates, Mech. Adv. Mater. Struct., vol. 19, no. 7, pp. 551–567, 2012. DOI: [10.1080/15376494.2011.563408](https://doi.org/10.1080/15376494.2011.563408).
- [35] S. Lore, A.S. Deshpande, and B.N. Singh, Nonlinear free vibration analysis of functionally graded plates and shell panels using quasi-3D higher order shear deformation theory, Mech. Adv. Mater. Struct., vol. 31, no. 2, pp. 453–469, 2024. DOI: [10.1080/15376494.2022.2114050](https://doi.org/10.1080/15376494.2022.2114050).
- [36] A. Gupta, M. Talha, and W. Seemann, Free vibration and flexural response of functionally graded plates resting on Winkler-Pasternak elastic foundations using nonpolynomial higher-order shear and normal deformation theory, Mech. Adv. Mater. Struct., vol. 25, no. 6, pp. 523–538, 2018. DOI: [10.1080/15376494.2017.1285459](https://doi.org/10.1080/15376494.2017.1285459).
- [37] S. Pal, M. Rout, and A. Karmakar, Thermoelastic free vibration of rotating tapered porous functionally graded conical shell based on non-polynomial higher-order shear deformation theory, Mech. Adv. Mater. Struct., vol. 31, no. 25, pp. 7469–7485, 2024. DOI: [10.1080/15376494.2023.2245820](https://doi.org/10.1080/15376494.2023.2245820).
- [38] E. Mohseni, A.R. Saidi, and M. Mohammadi, Bending-stretching analysis of thick functionally graded micro-plates using higher-order shear and normal deformable plate theory, Mech. Adv. Mater. Struct., vol. 24, no. 14, pp. 1221–1230, 2017. DOI: [10.1080/15376494.2016.1227503](https://doi.org/10.1080/15376494.2016.1227503).
- [39] S.S. Kolapkar and A.S. Sayyad, Static analysis of functionally graded shells of double curvature using trigonometric shear and normal deformation theory, Mech. Adv. Mater. Struct., pp. 1–27, 2024. DOI: [10.1080/15376494.2024.2445216](https://doi.org/10.1080/15376494.2024.2445216).
- [40] M. Shishehsaz, H. Raissi, and S. Moradi, Stress distribution in a five-layer circular sandwich composite plate based on the third and hyperbolic shear deformation theories, Mech. Adv. Mater. Struct., vol. 27, no. 11, pp. 927–940, 2020. DOI: [10.1080/15376494.2018.1502379](https://doi.org/10.1080/15376494.2018.1502379).
- [41] F. Ebrahimi and A. Jafari, A four-variable refined shear-deformation beam theory for thermo-mechanical vibration analysis of temperature-dependent FGM beams with porosities, Mech. Adv. Mater. Struct., vol. 25, no. 3, pp. 212–224, 2018. DOI: [10.1080/15376494.2016.1255820](https://doi.org/10.1080/15376494.2016.1255820).
- [42] A.-A. Daikh, M.-O. Belarbi, D. Ahmed, M.S.A. Houari, M. Avcar, A. Tounsi, and M.A. Eltaher, Static analysis of functionally graded plate structures resting on variable elastic foundation under various boundary conditions, Acta Mech., vol. 234, no. 2, pp. 775–806, 2023. DOI: [10.1007/s00707-022-03405-1](https://doi.org/10.1007/s00707-022-03405-1).
- [43] D.G. Ashwell and A.B. Sabir, A new cylindrical shell finite element based on simple independent strain functions, Int. J. Mech. Sci., vol. 14, no. 3, pp. 171–183, 1972. DOI: [10.1016/0020-7403\(72\)90074-4](https://doi.org/10.1016/0020-7403(72)90074-4).
- [44] A.B. Sabir and A. Sfendji, Triangular and rectangular plane elasticity finite elements, Thin-Walled Struct., vol. 21, no. 3, pp. 225–232, 1995. DOI: [10.1016/0263-8231\(94\)00002-H](https://doi.org/10.1016/0263-8231(94)00002-H).
- [45] L. Fortas, L. Belounar, and T. Merzouki, Formulation of a new finite element based on assumed strains for membrane structures, Int. J. Adv. Struct. Eng., vol. 11, no. S1, pp. 9–18, 2019. DOI: [10.1007/s40091-019-00251-9](https://doi.org/10.1007/s40091-019-00251-9).
- [46] M.S. Djoudi and H. Bahai, A cylindrical strain-based shell element for vibration analysis of shell structures, Finite Elem. Anal. Des., vol. 40, no. 13–14, pp. 1947–1961, 2004. DOI: [10.1016/j.finel.2003.11.008](https://doi.org/10.1016/j.finel.2003.11.008).
- [47] A. Belounar, ‘Eléments finis membranaires et flexionnels à champ de déformation pour l’analyse des structures’, doctoral, Université Mohamed Khider - Biskra, 2019. Accessed: Dec. 08, 2024. [Online]. Available from <http://thesis.univ-biskra.dz/4452/>
- [48] A. Belounar, F. Boussem, and A. Tati, A novel C0 strain-based finite element for free vibration and buckling analyses of functionally graded plates, J. Vib. Eng. Technol., vol. 11, no. 1, pp. 281–300, 2023. DOI: [10.1007/s42417-022-00577-x](https://doi.org/10.1007/s42417-022-00577-x).
- [49] M.T. Belarbi and A. Charif, Développement d’un nouvel élément hexaédrique simple basé sur le modèle en déformation pour l’étude des plaques minces et épaissees, Rev. Eur. Éléments Finis, vol. 8, no. 2, pp. 135–157, 1999. DOI: [10.1080/12506559.1999.10511361](https://doi.org/10.1080/12506559.1999.10511361).
- [50] L. Belounar and K. Guerraiche, A new strain based brick element for plate bending, Alex. Eng. J., vol. 53, no. 1, pp. 95–105, 2014. DOI: [10.1016/j.aej.2013.10.004](https://doi.org/10.1016/j.aej.2013.10.004).
- [51] K. Guerraiche, L. Belounar, and L. Bouzidi, A new eight nodes brick finite element based on the strain approach, J. Solid Mech., vol. 1, no. 1, p. 186, 2018.
- [52] H. Guenfoud, M. Himeur, H. Ziou, and M. Guenfoud, A consistent triangular thin flat shell finite element with drilling rotation based on the strain approach, Int. J. Struct. Eng., vol. 9, no. 3, pp. 191–223, 2018. DOI: [10.1504/IJSTRUCTE.2018.093673](https://doi.org/10.1504/IJSTRUCTE.2018.093673).
- [53] F. Boussem, A. Belounar, and L. Belounar, Assumed strain finite element for natural frequencies of bending plates, World J. Eng., vol. 19, no. 5, pp. 620–631, 2022. DOI: [10.1108/WJE-02-2021-0114](https://doi.org/10.1108/WJE-02-2021-0114).
- [54] A. Belounar, S. Benmebarek, M.N. Houhou, and L. Belounar, Static, free vibration, and buckling analysis of plates using strain-based Reissner–Mindlin elements, Int. J. Adv. Struct. Eng., vol. 11, no. 2, pp. 211–230, 2019. DOI: [10.1007/s40091-019-0226-4](https://doi.org/10.1007/s40091-019-0226-4).
- [55] A. Belounar, F. Boussem, M.N. Houhou, A. Tati, and L. Fortas, Strain-based finite element formulation for the analysis of functionally graded plates, Arch. Appl. Mech., vol. 92, no. 7, pp. 2061–2079, 2022. DOI: [10.1007/s00419-022-02160-y](https://doi.org/10.1007/s00419-022-02160-y).
- [56] M. Ramezani, M. Rezaiee-Pajand, and F. Tornabene, Linear and nonlinear mechanical responses of FG-GPLRC plates using a novel strain-based formulation of modified FSDT theory, Int. J. Non-Linear Mech., vol. 140, pp. 103923, 2022. DOI: [10.1016/j.ijnonlinmec.2022.103923](https://doi.org/10.1016/j.ijnonlinmec.2022.103923).
- [57] T. Assas, M. Bourezane, and M. Chenafi, Static, free vibration, and buckling analysis of functionally graded plates using the strain-based finite element formulation, Arch. Appl. Mech., vol. 94, no. 8, pp. 2243–2267, 2024. DOI: [10.1007/s00419-024-02635-0](https://doi.org/10.1007/s00419-024-02635-0).
- [58] T. Assas, M. Bourezane, M. Chenafi, and A. Tati, Static and free vibration response of FGM plates using higher order shear deformation theory and strain-based finite element formulation, Mech. Based Des. Struct. Mach., pp. 1–30, 2024. DOI: [10.1080/15397734.2024.2418828](https://doi.org/10.1080/15397734.2024.2418828).
- [59] D.-G. Zhang and Y.-H. Zhou, A theoretical analysis of FGM thin plates based on physical neutral surface, Comput. Mater. Sci., vol. 44, no. 2, pp. 716–720, 2008. DOI: [10.1016/j.commat.2008.05.016](https://doi.org/10.1016/j.commat.2008.05.016).
- [60] T. Prakash, M.K. Singha, and M. Ganapathi, Influence of neutral surface position on the nonlinear stability behavior of functionally graded plates, Comput. Mech., vol. 43, no. 3, pp. 341–350, 2009. DOI: [10.1007/s00466-008-0309-8](https://doi.org/10.1007/s00466-008-0309-8).
- [61] A.M. Zenkour and M.H. Aljadani, Mechanical buckling of functionally graded plates using a refined higher-order shear and normal deformation plate theory, Adv. Aircr. Spacecr. Sci., vol. 5, no. 6, Art. no. 6, Nov. 2018, Techno-Press, Daejeon, South Korea.